

1 Revision 1

2

3 New insights into the metallogeny of the Nayongzhi MVT Zn-Pb deposit in  
4 Guizhou Province (South China): Evidence from geology, bulk C-O-S and in  
5 situ S-Pb isotopes

6

7

8 JIA-XI ZHOU<sup>1, 2, \*</sup>, XUAN-CE WANG<sup>2</sup>, SIMON A. WILDE<sup>2</sup>, KAI LUO<sup>1, 3</sup>,  
9 ZHI-LONG HUANG<sup>1</sup>, TAO WU<sup>4</sup>, ZHONG-GUO JIN<sup>1</sup>

10

11

12 <sup>1</sup> *State Key Laboratory of Ore Deposit Geochemistry, Institute of*  
13 *Geochemistry, Chinese Academy Sciences, Guiyang 550081, China*

14 <sup>2</sup> *The Institute for Geoscience Research, Department of Applied Geology,*  
15 *Curtin University, GPO Box U1987, Perth, WA 6845, Australia*

16 <sup>3</sup> *University of Chinese Academy Sciences, Beijing 100049, China*

17 <sup>4</sup> *School of Earth Sciences, Zhejiang University, Hangzhou 310027, China*

18

19

20 \*Corresponding author, JIA-XI ZHOU, E-mail: [zhoujiaxi@vip.gyig.ac.cn](mailto:zhoujiaxi@vip.gyig.ac.cn)

21

22

23

## ABSTRACT

24 The newly-discovered Nayongzhi Zn-Pb deposit (> 20 Mt ores @ 1.11-15.65  
25 wt. % Zn and 0.59-0.97 wt. % Pb) in NW Guizhou province, South China, is  
26 hosted by late Ediacaran and early Cambrian carbonate rocks. Ore body is  
27 structurally controlled by a kilometer-scale reverse fault-anticline system and  
28 occurs as stratiform, lentiform or steeply dipping veined. Its geological feature  
29 can compare to that of the Mississippi Valley-type (MVT) Zn-Pb deposits.  $\delta^{34}\text{S}$   
30 values (+11.8-+33.0‰) of sulfide minerals determined by NanoSIMS have a  
31 larger range than those determined by conventional bulk analysis ( $\delta^{34}\text{S} =$   
32 +18.12-+24.79‰). This suggests that S isotopes determined by in situ analysis  
33 can reflect the nature of fractionation involved in mineralization. Further, cores  
34 of sulfide crystals have higher  $\delta^{34}\text{S}$  values (+26.1-+33.0‰) than their rims  
35 (+11.8-+24.5‰). This implies a mixture of multiple S reservoirs or a Rayleigh  
36 fractionation of S isotopes occurred during ore formation process. Additionally,  
37 both S isotopic compositions determined by in situ and bulk analyses reflect  
38 the enrichment of  $^{34}\text{S}$  in hydrothermal fluid ( $\delta^{34}\text{S}_{\text{fluid}} > +11.8\text{‰}$ ), a typical  
39 characteristic of marine sulfate-derived S. Such S isotopic signatures also  
40 show that thermochemical sulfate reduction (TSR) is the dominant mechanism  
41 for the incorporation of  $\text{S}^{2-}$  from  $\text{SO}_4^{2-}$ . Pb isotopic ratios of galena obtained by  
42 femtosecond LA-MC-ICPMS plot in the field that overlaps with the Pb evolution  
43 curve of upper crust contributed to the orogeny and the field of modern lower  
44 crust, and can be compared to the Proterozoic metamorphic rocks. The means

45 that the majority of Pb metal is sourced from the basement rocks. Although  
46  $\delta^{13}\text{C}$  values (-4.1-+0.5‰) of calcite separates and corresponding fluids are  
47 similar to both fresh limestone (-1.7-+1.3‰) and typical marine carbonate  
48 rocks, the  $\delta^{18}\text{O}$  values (+12.4-+14.1‰) are significantly lower than both  
49 limestone (+24.1-+25.5‰) and marine carbonate rocks. Such C-O isotopic  
50 characteristics suggest that the source of C is ore-hosting carbonate rocks,  
51 whereas O has a mixed source of metamorphic fluids and carbonate rocks  
52 resulting from water/rock (W/R) interaction. All in all, this study demonstrates  
53 that (i) fluid mixing caused rapid sulfide precipitation, resulting in significant  
54 fractionation of S isotopes; and (ii) both the W/R interaction and  $\text{CO}_2$   
55 degassing controlled local carbonate cyclic process of dissolution →  
56 re-crystallization, which provided metastable physical and chemical conditions  
57 for giant sulfide mineralization. These two processes are crucial in forming  
58 MVT deposits.

59 **Key words:** In situ S-Pb isotopes; Fluid mixing; Buffer of carbonate; MVT  
60 deposits; South China

61

62

## INTRODUCTION

63 Zn-Pb deposits hosted by carbonate or siliciclastic rocks contain the world's  
64 greatest Zn and Pb resources, and predominate the world production of these  
65 metals (e.g., [Leach et al. 2005](#)). They are known as sediment-hosted types of  
66 ore deposit and generally have no direct genetic association with igneous

67 activity (e.g., [Leach et al. 2010](#)). Carbonate-hosted Zn-Pb deposits, one of the  
68 two major subtypes of sediment-hosted Zn-Pb deposits, occur in platform  
69 carbonate sequences and are commonly named as the Mississippi Valley-type  
70 (MVT) deposits (e.g., [Leach et al. 2010](#)). Extensive research on the MVT  
71 deposits has dedicated greatly to our understanding of fluid flow and metal  
72 transport in sedimentary basin (e.g., [Heijlen et al. 2003](#); [Leach et al. 2005](#);  
73 [Wilkinson et al. 2009](#)). However, as the MVT deposits are the products of a  
74 variety of ore formation processes in a wide range of geologic and tectonic  
75 environments (e.g., [Wilkinson et al. 2009](#); [Leach et al. 2010](#)), so their ore  
76 genesis is still controversial, and the chemical and isotopic evolution of  
77 hydrothermal fluids also needs to be careful constrained.

78 In China, carbonate-hosted Zn-Pb deposits are widely distributed in the  
79 platform carbonate sequences surrounding the Yangtze Craton (e.g., [Zaw et al.](#)  
80 [2007](#); [Wang et al. 2014](#); [Hu et al. 2017](#)). For example, more than 400 Zn-Pb  
81 deposits in the western Yangtze Craton form the Sichuan-Yunnan-Guizhou  
82 (SYG) Pb-Zn metallogenic province ([Fig. 1A-B](#)) with more than 200 Mt ores  
83 grading 10-15 wt. % Zn + Pb (e.g., [Zhou et al. 2013a, 2014a](#)). Such a province  
84 is an important part of the giant South China low-temperature metallogenic  
85 domain (e.g., [Hu et al. 2017](#)), accounting for 27% of total Zn + Pb resources in  
86 China ([Zhang et al. 2015](#)). Extensive investigation on the origin of the Zn-Pb  
87 deposits in the SYG province has been carried out in the past two decades,  
88 although they belong to epigenetic type is widely recognized, there is still a

89 struggle of ore genesis, such as MVT (e.g., [Zheng and Wang 1991](#); [Zhou et al.](#)  
90 [2001](#); [Wang et al. 2014](#); [Zhang et al. 2015](#); [Zhu et al. 2017](#)), distal  
91 magmatic-hydrothermal type (e.g., [Xie, 1963](#); [Huang et al. 2010](#); [Bai et al.](#)  
92 [2013](#); [Xu et al. 2014](#)) or unique SYG-type (e.g., [Zhou et al. 2013b, 2014b](#); [Li et](#)  
93 [al. 2015, 2016](#); [Zhu et al. 2016](#)).

94 Micro-beam analytical techniques have potential to provide key in situ  
95 elemental and isotopic information to constrain the sources of mineralizing  
96 elements and associated fluids, as well as the metallogenic environments of  
97 the hydrothermal system (e.g., [Liu et al. 2008](#); [Barker et al. 2009](#); [Steinboefel](#)  
98 [et al. 2009](#); [Ye et al. 2011](#); [Zhang et al. 2014](#); [Yuan et al. 2015](#); [Jin et al. 2016](#)).

99 Such information is crucial for understanding the metallogeny of hydrothermal  
100 deposits. Secondary ion mass spectroscopy (SIMS) and laser-ablation  
101 multi-collector inductively coupled plasma mass spectrometry (LA-MC-ICPMS)  
102 are techniques that can efficiently determine micro-scale isotopic compositions  
103 of sulfide minerals in hydrothermal deposits (e.g., [Peevler et al. 2003](#); [Ikehata](#)  
104 [et al. 2008](#); [Chen et al. 2014](#); [Bao et al. 2016](#)).

105 Here we use the newly-discovered Nayongzhi MVT Zn-Pb deposit that situates  
106 in the southeastern part of the SYG province as a case, and report a set of  
107 NanoSIMS in situ S, femtosecond LA-MC-ICPMS in situ Pb, and conventional  
108 whole-rock C and O isotopic data. Through integrating the newly obtained data  
109 and detailed ore deposit geology, this study aims to reveal the origin and  
110 evolution of hydrothermal fluids, and then to propose a new genetic model for

111 the Nayongzhi deposit. The outcomes are crucial for understanding the  
112 formation and exploration of MVT deposits in general.

113

## 114 **GEOLOGICAL SETTING**

### 115 **General geology of the western Yangtze Craton**

116 The Yangtze Craton constitutes a significant part of the South China Block,  
117 and is bounded by the Cathaysia Block to the southeast, the Qinling-Dabie  
118 Orogenic Belt to the north, the Songpan-Ganzê Orogenic Belt to the northwest,  
119 and the Sanjiang Orogenic Belt to the southwest ([Fig. 1A](#)). The basement of  
120 the western Yangtze Craton consists of late Paleoproterozoic to early  
121 Neoproterozoic weakly metamorphic rocks, which were intruded by  
122 widespread late Neoproterozoic igneous rocks (e.g., [Qiu et al. 2000](#); [Zhou et al.](#)  
123 [2002, 2014c](#); [Gao et al. 2011](#)). The sedimentary succession of the western  
124 Yangtze Craton is composed mainly of Cambrian to Triassic marine and  
125 Jurassic to Cenozoic continental sedimentary rocks (e.g., [Yan et al. 2003](#);  
126 [Zhou et al. 2013a](#); [Hu et al. 2017](#)). Sulfate-bearing evaporates are common in  
127 the Cambrian to Triassic marine sedimentary strata, which are an important S  
128 source for the sediment-hosted hydrothermal deposits in the western Yangtze  
129 Craton (e.g., [Bai et al. 2013](#); [Zhou et al. 2014a](#); [Chen et al. 2015](#)). Faults in the  
130 western Yangtze Craton are well-developed and have undergone multi-stage  
131 activities (namely Hercynian, Indosinian, and Yanshanian orogenic events,  
132 and even Himalayan Orogeny), which dominantly controlled the sedimentation,

133 magmatism and mineralization (e.g., [Liu and Lin 1999](#)), such as the regional  
134 NW-trending Yiliang-Shuicheng and NS-trending Xiaojiang faults ([Figs. 1B,](#)  
135 [2-3](#)).

136 A significant feature of the western Yangtze Craton is the occurrence of  
137 Emeishan Large Igneous Province (ELIP) and its flood basalts (ca. 260 Ma)  
138 with an area of more than 250,000 km<sup>2</sup> (e.g., [Zhou et al. 2002](#); [Jian et al. 2009](#)).  
139 After eruption of late Permian Emeishan basalts, the western Yangtze Craton  
140 collided with the adjacent blocks (for example, Yidun Arc), resulting in the  
141 closure of the Paleo-Tethys ocean (e.g., [Reid et al. 2007](#); [Hu and Zhou 2012](#);  
142 [Zhou et al. 2013a](#); [Qiu et al. 2016](#); [Hu et al. 2017](#)). This event is named as the  
143 Indosinian Orogeny (257-205 Ma) (e.g., [Carter et al. 2001](#)). After then, there is  
144 the Yanshanian Orogeny that occurred during Jurassic-Cretaceous (205-135  
145 Ma) time (e.g., [Wong 1927](#)). These two orogenic events resulted in faulting  
146 and folding that significantly controlled the distribution of carbonate-hosted  
147 Zn-Pb deposits in the western Yangtze Craton (e.g., [Liu and Lin 1999](#); [Huang](#)  
148 [et al. 2010](#); [Zhou et al. 2014b](#); [Zhang et al. 2015](#)).

149 Another significant feature of the western Yangtze Craton is the occurrence of  
150 the SYG Zn-Pb mineralization province and its 408 Zn-Pb deposits with an  
151 area of more than 170,000 km<sup>2</sup> (e.g., [Liu and Lin 1999](#); [Zhou et al. 2014a](#); [Hu](#)  
152 [et al. 2017](#)). All the Zn-Pb deposits host in the late Ediacaran to middle  
153 Permian carbonate rocks and are spatially associated with the late Permian  
154 Emeishan basalts ([Fig. 1B](#)). Calcite/fluorite Sm-Nd, sphalerite/pyrite Rb-Sr and

155 bitumen Re-Os isotope geochronology studies suggest that these  
156 carbonate-hosted Zn-Pb deposits formed between 226 Ma and 165 Ma (e.g.,  
157 [Li et al. 2007](#); [Lin et al. 2010](#); [Mao et al. 2012](#); [Zhou et al. 2013a, 2013b, 2015](#);  
158 [Zhang et al. 2015](#); [Hu et al. 2017](#)). This indicates that the Zn-Pb mineralization  
159 in the SYG province occurred during late Triassic-middle Jurassic, and related  
160 to the Indosinian and Yanshanian two orogenic events.

### 161 **Regional geology of the NW Guizhou district**

162 The newly-discovered Nayongzhi carbonate-hosted Zn-Pb deposit is located  
163 in NW Guizhou province ([Figs. 1B, 2-3](#)). In the NW Guizhou district, the  
164 basement rocks of the western Yangtze Craton are not exposed ([Figs. 2-3](#)).  
165 The cover sequences including late Ediacaran to Triassic marine and Jurassic  
166 continental sedimentary rocks, as well as late Permian Emeishan continental  
167 flood basalts. The late Ediacaran strata consist mainly of limestone and  
168 dolostone. The Cambrian strata are composed dominantly of siltstone,  
169 claystone, limestone, argillaceous dolostone and dolomitic sandstone. These  
170 sedimentary rocks of late Ediacaran and Cambrian are unconformable overlain  
171 by Devonian strata that consist predominantly of sandstone, siltstone, shale,  
172 limestone and dolostone. The Devonian sedimentary rocks are conformably  
173 overlain by Carboniferous strata, which are composed mainly of shale,  
174 limestone and dolostone. The early-middle Permian sequence consists  
175 dominantly of sandstone, shale, coal layers and limestone, all of which are  
176 unconformable overlain by the late Permian Emeishan flood basalts. The



177 basalts, in turn, are overlain by sandstone, siltstone and coal measures of the  
178 late Permian strata. The Triassic strata consist mainly of siltstone, sandstone,  
179 dolostone and limestone, and the Jurassic strata are dominated by sandstone.  
180 The Zn-Pb sulfide ores are hosted by the late Ediacaran to middle Permian  
181 carbonate rocks and parts of them have a spatial association with late Permian  
182 basalts (e.g., [Jin 2008](#); [Zhou et al. 2013a](#); [Li et al. 2015](#); [Figs. 1B, 2-3](#)).

183 NW- and NE-striking faults and folds are well-developed in the NW Guizhou  
184 district, for example, the NW-trending Yadu-Ziyun fault ([Figs. 1B, 2-3](#)), the  
185 NE-trending Nayong-Kaiyang and Anshun-Pingba faults, and the NE-trending  
186 Dayuan and Wuzhishan anticlines ([Figs. 2-3](#)). Among these structures, the  
187 Yadu-Ziyun regional fault controlled the sedimentation and low temperature  
188 mineralization (Zn-Pb, Au and fluorite deposits) in the studied region ([Figs.](#)  
189 [2-3](#)). Mafic dykes (diabase), related to the ELIP (e.g., [Jin 2008](#)), also occur in  
190 this district and spatially associate with parts of Zn-Pb deposits ([Fig. 2](#)).

191 More than 100 carbonate-hosted Zn-Pb deposits have been found in the NW  
192 Guizhou district, such as the Tianqiao and Shanshulin deposits ([Figs. 1B, 2-3](#);  
193 [Jin 2008](#); [Zhou et al. 2013a, 2014b](#)). The Nayongzhi Zn-Pb deposit,  
194 discovered in 2011, occurs in the southeastern part of the NW Guizhou district  
195 ([Figs. 2-3](#)) and is hosted by limestone and dolostone of late Ediacaran  
196 Dengying Formation and early Cambrian Qingxudong Formation ([Figs. 4-6](#)).

197 This deposit is the largest and only large-scale (>0.5 Mt Zn + Pb metal reserve)  
198 carbonate-hosted Zn-Pb deposit in the Guizhou part of the SYG province ([Jin](#)

199 [et al. 2016](#)), containing Zn + Pb metal reserve of more than 1.5 Mt with ore  
200 grades of 1.11-15.65 wt. % Zn and 0.59-0.97 wt. % Pb.

201

## 202 **GEOLOGY OF THE NAYONGZHI ZN-PB DEPOSIT**

### 203 **Stratigraphy and lithology**

204 The Nayongzhi deposit is situated in the central part of the Wuzhishan  
205 anticline ([Figs. 2-4](#)). In the Wuzhishan anticline area, the exposed strata are  
206 late Ediacaran, Cambrian, early Carboniferous, early Permian and early  
207 Triassic ([Figs. 4-5](#)). The late Ediacaran Dengying Formation consists mainly of  
208 limestone and dolostone, which are conformable overlain by the early  
209 Cambrian Jindingshan Formation that is composed dominantly of siltstone and  
210 shale. Followed the Jindingshan Formation is the early Cambrian Qingxudong  
211 Formation, which is mainly made up of limestone and dolostone. The middle  
212 Cambrian Douposi Formation is composed predominantly of dolostone and  
213 sandstone, and the late Cambrian Loushanguan Formation is dominated by  
214 limestone and dolostone. The early Carboniferous strata comprise the  
215 Xiangbai and Jiusi formations, which consist mainly of limestone and siltstone,  
216 and shale and limestone, respectively. The early Permian Liangshan  
217 Formation consists dominantly of shale and sandstone, and the early Triassic  
218 Daye Formation is mainly made up of limestone. In the Nayongzhi mining area,  
219 the exposed strata are Qingxudong Formation ([Fig. 4](#)) that can be subdivided  
220 into three sections based on the lithological feature, of which the 1st and 2nd

221 sections have six and two lithological layers, respectively (Fig. 5). Zn-Pb ores  
222 host in the limestone and dolostone of the Dengying Formation, and the 1st  
223 section and the 1st layer of the 2nd section of the Qingxudong Formation (Figs.  
224 5, 6A-B).

## 225 **Tectonics**

226 In the Wuzhishan anticline area, the tectonics are well-developed and strictly  
227 control the distribution of Zn-Pb deposits (Figs. 3-4). The Wuzhishan anticline,  
228 a NE-trending asymmetric anticline, is 16 km long and 4 km wide with an axis  
229 trending angle of 45° (Fig. 4). The Narun fault (F<sub>1</sub> in Fig. 4), a normal structure,  
230 strikes NE and dips at SE. This fault intersects the Yadu-Ziyun regional fault to  
231 the southwest (Fig. 3). The Dujiqiao fault (F<sub>2</sub> in Fig. 4) is a reverse fault that  
232 strikes 30° and dips at SE with a dipping angle of 60°-70°. Another important  
233 fault, F<sub>7</sub> reverse fault (Fig. 4), trends north with a dipping angle of 51°-75°.  
234 Studies suggest that the Wuzhishan anticline, and NE- and NW-trending faults  
235 were active during the Yanshanian Orogeny (e.g., Chen et al. 2015). In the  
236 Nayongzhi ore district, sulfide ore is structurally controlled by a reverse  
237 fault-anticline system, namely the F<sub>7</sub> reverse fault and Wuzhishan anticline  
238 (Figs. 4, 6A-B).

## 239 **Ore body**

240 In the Nayongzhi ore district, one steeply dipping veined and twenty stratiform  
241 or lentiform ore bodies have been found in total until 2015 (Peng et al. 2016).  
242 The steeply dipping veined ore body occurs along the F<sub>7</sub> reverse fault zone

243 (Figs. 6A, 7E), which is 20-50 m long, 0.5-3 m wide and 200 m thick. This ore  
244 body contains high ore grade of Zn (> 10 wt. %), with less abundant Pb. The  
245 stratiform or lentiform ore bodies (Figs. 6A-B, 7A) can be combined into three  
246 groups (I, II and III) based on the lithological character of their ore-bearing  
247 layers (Figs. 5, 6A-B). Ore bodies in these three groups are similar, of which  
248 the Group II is the largest and occurs in the 5th layer of the 1st section of the  
249 Qingxudong Formation (Figs. 5, 6A-B). Here we take the Group II as an  
250 example to introduce the geology of ore body. Sulfide ore in this group is  
251 hosted by limestone and dolostone, with argillaceous limestone and dolostone  
252 as wall rocks. The ore bodies are stratiform or lentiform and have the same  
253 orientation as the ore-hosting rocks, namely strike NE and dip SE with a  
254 dipping angle of 8°-20°. The main ore body in the Group II is 2725 m long,  
255 250-775 m wide and 1-29.6 m thick, containing 0.5-36.63 wt. % Zn (average  
256 4.03 wt. %) and 0.04-4.05 wt. % Pb (average 0.45 wt. %). This ore body  
257 contains Zn + Pb metal reserve of more than 0.5 Mt and is the largest one in  
258 the Nayongzhi deposit.

### 259 **Texture and structure of sulfide ores**

260 Sulfide ore in the Nayongzhi deposit consists mainly of sphalerite, secondary  
261 galena and pyrite, with calcite or dolomite as primary gangue minerals, and  
262 rare quartz or barite as local associated minerals (Figs. 7-10).

263 Sulfide ore in veined, stratiform or lentiform ore bodies occurs as either veined  
264 (Figs. 7B, D, G, J-K, M, O, 8H, J, L-P), massive (Figs. 7C, K, N, 8D-F, I), or

265 disseminated (Figs. 7H, 8A-C, G, L). Their general feature is as follows: (i)  
266 Veined ore: sulfide minerals (sphalerite, galena and pyrite) occur as veinlet or  
267 stockwork, and fill into fracture or cement carbonate solution collapse breccia  
268 (such as Fig. 7B, D, G); (ii) Massive ore: sulfide minerals form massive  
269 aggregation in wall rocks (for example, Figs. 7C, 8D-E); and (iii) Disseminated  
270 ore: sulfide minerals present as speckle aggregation that densely or sparsely  
271 distributes in wall rocks (e.g. Figs. 7H, 8A-C, G). Syn- or post-ore gangue  
272 minerals occur as crumb or veined aggregation that fills into fracture or  
273 cements carbonate breccia (such as Fig. 7B-C, F, H).

274 Sulfide minerals have granular, fragmented or replacement textures (Figs.  
275 9-10), which have general feature as following: (i) Granular texture: sphalerite  
276 presents as fine to coarse (0.01-10 mm) granular crystal that coexists with  
277 pyrite (Figs. 9C, F-H, 10C-E, H-J), galena (Figs. 9D, F-G, J-K, N-O, 10B, G-H,  
278 K-N), quartz (Fig. 9D), or calcite/dolomite (Figs. 9A, D, J-K, M-O, 10B, D, F, G-I,  
279 L-P), and is enclosed by pyrite (Fig. 9B), galena (Fig. 9O, 10A) or  
280 calcite/dolomite (Figs. 9A-C, E-F, 10C, G-J, L, N-O); galena occurs as fine to  
281 medium (0.05-0.6 mm) granular crystal, coexisting with sphalerite (Figs. 9D,  
282 F-G, J-K, N-O, 10B-C, G-H, L-N) and is enclosed by calcite/dolomite (Figs. 9F,  
283 K, 10A, G-H, K-L, N), sphalerite (Fig. 10L, O) or pyrite (Fig. 10I); pyrite occurs  
284 as fine (0.001-0.2 mm) granular crystal, coexisting with sphalerite (Figs. 9A-C,  
285 F-H, 10C-F, H-J) and is enclosed by calcite/dolomite (Figs. 9C, 10J), galena  
286 (Fig. 10A) or sphalerite (Fig. 10P). Diagenetic pyrite is fine-grained and

287 distributes in wall rocks (Fig. 8K) or is cemented by quartz (Fig. 9L) (ii)  
288 Fragmented texture: fragmented sphalerite is enclosed by pyrite (Fig. 10D) or  
289 calcite/dolomite (Fig. 10J) and is filled by galena (Fig. 10K) or calcite/dolomite  
290 (Fig. 10P); and (iii) Replacement texture: sphalerite is replaced by galena (Fig.  
291 9H) or replaces pyrite (Figs. 9M, 10F).

## 292 **Mineral paragenesis**

293 The Nayongzhi carbonate-hosted Zn-Pb deposit has experienced diagenetic,  
294 hydrothermal and oxidized periods (Table 1), of which the hydrothermal period  
295 can be further subdivided into sulfide + (quartz + calcite/dolomite) and quartz +  
296 calcite/dolomite + (barite) stages (Figs. 7-10). There are two principal types of  
297 sulfide ore formed during the sulfide stage: sphalerite-dominated + pyrite +  
298 galena + quartz + calcite/dolomite, and sphalerite- and galena-dominated +  
299 pyrite + quartz + calcite/dolomite. The spatial distribution of sulfide ore (Fig. 7)  
300 shows the formation sequence is from sphalerite-dominated massive (Fig. 8D,  
301 I) or dense disseminated ore (Fig. 8A-C, L), and sphalerite- and  
302 galena-dominated massive (Fig. 8E-F) or sparse disseminated ore (Fig. 8G), to  
303 metasomatic, filled or cemented ore vein (Fig. 8H, J, L-P). Therefore, sulfide  
304 minerals have two generations. Sphalerite-I is fine- to medium-grained  
305 (0.02-0.6) mm, coexisting with pyrite-I (Figs. 8D, 9A, C, G-H, 10C, E, J) or  
306 galena-I (Figs. 8C, 10C), and is enclosed by pyrite-II (Figs. 9B, 10D) or  
307 galena-II (Figs. 9O, 10A), as well as is replaced by galena-II (Fig. 9H);  
308 Sphalerite-II is medium to coarse granular crystal (0.5-10 mm) that coexists

309 with pyrite-II (Figs. 9B, F, 10D, H-I) or galena-II (Figs. 9D, F, J-K, N-O, 10B,  
310 G-H, L-O), and is enclosed by calcite-II (Fig. 9E, 10G-I, N-O) and also replaces  
311 pyrite-I (Figs. 9M, 10F). Galena-I is fine- to medium-grained (0.05-0.2 mm),  
312 coexisting with pyrite-I or sphalerite-I (Figs. 8C, 10C), and is enclosed by  
313 sphalerite-II (Figs. 9I, 10L), pyrite-II (Fig. 10I) or calcite-II (Fig. 10K); Galena-II  
314 is medium to coarse granular crystal (0.1-0.6 mm) that coexists with  
315 sphalerite-II (Figs. 9D, F, J-K, N-O, 10B, G-H, L-O) or pyrite-II (Fig. 10H), and  
316 is enclosed by calcite-II (Fig. 10G, N), as well as replaces sphalerite-I (Fig. 9H).  
317 Pyrite-I coexists with sphalerite-I (Figs. 8D, 9A, C, G-H, 10C, E, J) or pyrite-I  
318 (Fig. 10C), and is enclosed by galena-II (Fig. 10A) or sphalerite-II (Fig. 10P),  
319 and also is replaced by sphalerite-II (Figs. 9M, 10F); Pyrite-II coexists with  
320 sphalerite-II (Figs. 9B, F, 10D, H-I) or galena-II (Fig. 10H), and encloses  
321 sphalerite-I (Fig. 9B). In addition, calcite/dolomite-I is rare (Figs. 9A, H-I, 10E,  
322 J-K); Calcite/dolomite-II fills or cements sphalerite-I, galena-I or pyrite-I (Figs.  
323 9A-C, G, 10C, E, J-K), and coexists with pyrite-II, sphalerite-II or galena-II  
324 (Figs. 9D-E, J-K, N-O, 10B, D, L-M); Calcite/dolomite-III occurs as crumb,  
325 veinlet or stockwork that fills into fractures of sulfide ore (Figs. 7B-C, 8G, 9C)  
326 or cements carbonate breccia (Fig. 7C, F, H).

### 327 **Wall rock alteration**

328 Wall rock alteration includes dolomitization (dolomite), calcitization (calcite),  
329 silicification (quartz) and baritization (barite). These alteration styles can be  
330 divided into two stages: (i) pre-ore stage of carbonatization that formed

331 re-crystallized Fe-/Mn-bearing dolostone (Fig. 7A), and silicification that  
332 generated banded quartz or silicified dolostone (Fig. 7M); and (ii) post-ore  
333 stage of carbonatization, silicification and baritization that formed carbonate  
334 veinlet or stockwork (dolomite and calcite) (Fig. 7C, H-I, L), quartz and barite  
335 vein (Fig. 7F, P), respectively. The pre-ore alteration is the result of water/rock  
336 interaction between hydrothermal fluids and wall rocks, and then resulted in  
337 elemental and isotopic exchange. This type of alteration occurs commonly  
338 along the structure for fluid migration. The post-ore alteration is the result of  
339 late evolution of hydrothermal fluids and is generally close to sulfide ore, and  
340 thus can be used as a cue for ore exploration.

341

## 342 **SAMPLES AND ANALYTICAL METHODS**

### 343 **Samples**

344 Samples were collected from the exploration engineering of the Nayongzhi  
345 Zn-Pb deposit, including drill holes and underground mining tunnels (Figs. 7-8).  
346 Seven calcite and sixteen sulfide minerals (pyrite and sphalerite) separates  
347 were handpicked from twenty-three sulfide ore samples by micro-drill and  
348 binocular microscope. Five limestone whole-rock samples were also collected  
349 for C and O isotope analyzing. Five polished thin sections of sulfide ore were  
350 used for in situ S and Pb isotope analyzing. In situ S isotopic composition of  
351 galena was not determined as no galena standard is available for comparison  
352 (Zhang et al. 2014). In addition, in situ Pb isotopic composition of sphalerite



353 and pyrite was not determined, because of the high Hg content of them could  
354 significantly affect the quality of the obtained Pb isotopic data (Chen et al.  
355 2014).

## 356 **Analytical methods**

### 357 (I) Bulk C and O isotope analyses

358 Bulk C and O isotope analyses were completed by using a Finnigan MAT-253  
359 mass spectrometer at the State Key Laboratory of Ore Deposit Geochemistry  
360 (SKLOGD), Institute of Geochemistry (IG), Chinese Academy Sciences (CAS).  
361 Calcite and whole-rock limestone reacted with 100% phosphoric acid ( $H_3PO_4$ )  
362 to produce  $CO_2$ . The analytical precision calculated from replicate analyses of  
363 unknown samples is better than 0.2‰ ( $2\sigma$ ) for  $\delta^{13}C$  and 1‰ ( $2\sigma$ ) for  $\delta^{18}O$ . The  
364 C and O isotopic ratios are reported relative to Vienna Pee Dee Belemnite  
365 (V-PDB).

### 366 (II) Bulk S isotope analysis

367 Bulk S isotopic composition was analyzed by using a Finnigan MAT-253 mass  
368 spectrometer at the SKLOGD, IGCAS. Powder of sulfide separate finer than  
369 200 mesh was mixed with CuO powder, and then heated to extract  $SO_2$  gas.  
370 The  $^{34}S/^{32}S$  ratios are expressed by the conventional  $\delta^{34}S$  value in per mil  
371 relative to the Vienna Canyon Diablo Troilite (V-CDT) standard. The analytical  
372 error is better than 0.1‰ ( $1\sigma$ ) calculated from replicate analyses of the IAEA  
373 international standards: IAEA S1 (-0.3‰), IAEA S2 (+22.62‰) and IAEA S3  
374 (-32.49‰). The precision calculated from replicate analyses of unknown

375 samples is better than 0.2‰ ( $2\sigma$ ).

376 (III) In situ S isotope analysis

377 In situ S isotopic composition was performed by using a CAMECA NanoSIMS  
378 50 L at the Key Laboratory of Earth and Planetary Physics, IGGCAS. The  
379 measurement was made using three different settings of the Faraday cup (FC)  
380 and/or electron multiplier (EM) detector, which meet different requirements for  
381 spatial resolution. The effect of EM aging and quasi-simultaneous arrival was  
382 corrected before the calibration of instrumental mass fractionation by a  
383 standard-sample-standard bracketing method using the standards measured  
384 together with the samples. Target spot of the most homogeneous isotopic  
385 composition (such as  $^{32}\text{S}$ ,  $^{34}\text{S}$  and  $^{75}\text{As}$  in [Fig. 15B](#)) was selected for S isotope  
386 analyzing in order to obtain the credible in situ S isotopic data. International  
387 standards included Balmat (pyrite and sphalerite) and CAR 123 (pyrite), and  
388 internal standards included PY-1117 (pyrite), CS01 (pyrite), JC-14 (sphalerite)  
389 and MY09-12 (sphalerite). The analytical precision calculated from replicate  
390 analyses of unknown samples is better than 0.2‰ (1s). The detail of  
391 NanoSIMS in situ S isotope analysis and instrument parameter was described  
392 in the reference of [Zhang et al. \(2014\)](#).

393 (IV) In situ Pb isotope analysis

394 In situ Pb isotopic ratio was determined by using a Nu II MC-ICPMS (Nu  
395 Instruments, Wrexham, UK) combined with a 266 nm NWR UP Femto  
396 femtosecond (fs) laser ablation system (ESI, USA) at the State Key Laboratory

397 of Continental Dynamics, Northwest University. The surface of the polished  
398 thin section was cleaned with milli-Q water (18.2 M $\Omega$ ·cm). Line scan ablation  
399 consisted of background collection for 20 s followed by 50 s of laser ablation  
400 for signal collection. Laser ablation parameter is as follows: (i) spot size: 15  $\mu$ m  
401 for galena; (ii) 100% output energy: > 600  $\mu$ J; (iii) 100% energy density: 6  
402 J/cm<sup>2</sup>; (iv) laser frequency: 5-50 Hz; and (v) ablation way: line 3  $\mu$ m/s. This  
403 ensures a strong enough Pb signal for the analyses of sulfide samples. The TI  
404 (20 ppb, NIST SRM 997, <sup>205</sup>Tl/<sup>203</sup>Tl = 2.38890) and NIST SRM 610 glass were  
405 served as internal and external standards, respectively. The repeated analyses  
406 of NIST SRM 610 glass standard yielded highly reliable and reproducible  
407 results during the whole analytical process with mean <sup>206</sup>Pb/<sup>204</sup>Pb, <sup>207</sup>Pb/<sup>204</sup>Pb  
408 and <sup>208</sup>Pb/<sup>204</sup>Pb ratios of 17.052  $\pm$  0.003, 15.515  $\pm$  0.003 and 36.980  $\pm$  0.007  
409 (1s, *n* = 183), respectively. The detail of fs LA-MC-ICPMS in situ Pb isotope  
410 analysis and instrument parameter was described in the references of [Chen et](#)  
411 [al. \(2014\)](#) and [Bao et al. \(2016\)](#).

412

413

## ANALYTICAL RESULTS

### 414 Carbon and Oxygen isotopic composition

415 Carbon and Oxygen isotopic data of limestone whole-rock samples and  
416 syn-ore calcite separates are presented in [Table 2](#), and are shown in [Figures](#)  
417 [11-13](#). Limestone samples have  $\delta^{13}\text{C}$  and  $\delta^{18}\text{O}$  values ranging from -1.7 to  
418 +1.3‰ and +24.1 to +25.5‰, respectively. Calcite separates have  $\delta^{13}\text{C}$  values

419 ranging from -4.1 to +0.5‰ and  $\delta^{18}\text{O}$  values from +12.4 to +14.1‰. The  
420 calcite-II separates have higher  $\delta^{13}\text{C}$  values (-1.9-+0.5‰) and lower  $\delta^{18}\text{O}$   
421 values (+12.4-+13.6‰) than that of calcite-III separate ( $\delta^{13}\text{C} = -4.1‰$  and  $\delta^{18}\text{O}$   
422 = +14.1‰). A marked negative relationship between  $\delta^{13}\text{C}$  and  $\delta^{18}\text{O}$  values of  
423 all the calcite separates is shown in [Figure 11](#).

#### 424 **Bulk and in situ S isotopic composition**

425 Bulk and in situ S isotopic data are listed in [Table 3](#), and are shown in [Figures](#)  
426 [14-15](#). Sulfide separates have bulk  $\delta^{34}\text{S}$  values ranging from +17.17 to  
427 +24.79‰, of which pyrite and sphalerite separates have  $\delta^{34}\text{S}$  values ranging  
428 from +18.12 to +22.06‰ and +17.17 to +24.79‰, respectively. In addition,  
429 bulk  $\delta^{34}\text{S}$  values (+22.51-+24.79‰) of sphalerite-I overlap with those of  
430 sphalerite-II ( $\delta^{34}\text{S} = +17.17$ -+24.59‰). The NanoSIMS in situ  $\delta^{34}\text{S}$  values of  
431 sulfide crystals range from +11.8 to +33.0‰, of which pyrite and sphalerite  
432 crystals have in situ  $\delta^{34}\text{S}$  values ranging from +15.1 to +27.0‰ and +11.8 to  
433 +33.0‰, respectively. As shown in [Figure 14C](#), in situ S isotopic data have a  
434 much wider range than bulk S isotopic data. A significant feature of both  
435 sphalerite and pyrite crystals is that the in situ  $\delta^{34}\text{S}$  values decrease from core  
436 to rim (sphalerite: decreasing from +33.0 to +11.8‰; pyrite: decreasing from  
437 +27.0 to +15.1‰; [Fig. 15A](#)).

#### 438 **In situ Pb isotopic ratio**

439 In situ Pb isotopic ratios of galena are presented in [Table 4](#), and are shown in  
440 [Figures 16-18](#). Galena crystals have in situ Pb isotopic ratios as follows:

441  $^{206}\text{Pb}/^{204}\text{Pb} = 17.83\text{-}17.87$ ,  $^{207}\text{Pb}/^{204}\text{Pb} = 15.65\text{-}15.67$  and  $^{208}\text{Pb}/^{204}\text{Pb} =$   
442  $37.92\text{-}38.00$  with  $\mu$  ( $^{238}\text{U}/^{204}\text{Pb}$ ) values of  $9.64\text{-}9.67$ . The galena-I (fine-grained)  
443 crystals have  $^{206}\text{Pb}/^{204}\text{Pb}$  ratios of  $17.83\text{-}17.84$ ,  $^{207}\text{Pb}/^{204}\text{Pb}$  ratios of  
444  $15.65\text{-}15.67$  and  $^{208}\text{Pb}/^{204}\text{Pb}$  ratios of  $37.92\text{-}37.97$ , which are slightly lower  
445 than those of galena-II crystals (coarse-grained) ( $^{206}\text{Pb}/^{204}\text{Pb} = 17.84\text{-}17.87$ ,  
446  $^{207}\text{Pb}/^{204}\text{Pb} = 15.65\text{-}15.67$ , and  $^{208}\text{Pb}/^{204}\text{Pb} = 37.93\text{-}38.00$ ) (Fig. 17A-B).

447

448

## DISCUSSION

### 449 Source of mineralizing elements

450 (I) Source of  $\text{CO}_2$  and mechanism of calcite precipitation

451 (i) Source of  $\text{CO}_2$

452 Carbon and oxygen isotopic composition of  $\text{CO}_2$  of different origins are distinct.

453 For example, mantle-derived  $\text{CO}_2$  has  $\delta^{13}\text{C}$  values ranging from  $-8$  to  $-4\text{‰}$  and

454  $\delta^{18}\text{O}$  values from  $+6$  to  $+10\text{‰}$  (e.g., Taylor et al. 1967; Demény et al. 1998),

455 whereas marine carbonate rocks-derived  $\text{CO}_2$  has  $\delta^{13}\text{C} = -4\text{‰}$  and  $\delta^{18}\text{O} =$

456  $+20\text{‰}$  to  $+30\text{‰}$  (e.g., Veizer and Hoefs 1976), and the  $\delta^{13}\text{C}$  and  $\delta^{18}\text{O}$  values of

457 sedimentary organic matter-derived  $\text{CO}_2$  range from  $-30$  to  $-15\text{‰}$  and  $+24$  to

458  $+30\text{‰}$ , respectively (e.g., Hoefs 2009).

459 Calcite and dolomite are the two main C-bearing hydrothermal minerals in the

460 Nayongzhi sulfide ore (Figs. 6-7). Therefore,  $\text{H}_2\text{CO}_3$  [present as  $\text{CO}_2$

461 (aqueous)] and  $\text{HCO}_3^-$  are two key C species in hydrothermal fluids as

462 evidenced by fluid inclusion observation (Zhu et al. 2016). Given that the C

463 isotope fractionation between  $\text{H}_2\text{CO}_3$  or  $\text{HCO}_3^-$  (liquid) and  $\text{CO}_2$  (gas) is  
464 negligible, i.e.  $\delta^{13}\text{C}_{\text{fluid}} \approx \delta^{13}\text{C}_{\text{CO}_2}$  (Ohmoto 1972), we could obtain the  
465 theoretical  $\delta^{13}\text{C}_{\text{fluid}}$  value according to the calculated  $\delta^{13}\text{C}_{\text{CO}_2}$  value.

466 With an average homogenization temperature of  $180^\circ\text{C}$  (fluid inclusions in  
467 quartz-II that formed synchronously with calcite-II; Zhu et al. 2016), the  $\delta^{13}\text{C}_{\text{CO}_2}$   
468 values that range from  $-4.2$  to  $+0.4\text{‰}$  were calculated by using the function of  
469  $1000\ln\alpha_{(\text{CO}_2\text{-Calcite})} = -2.4612 + 7.663 \times 10^3 / (t + 273.15) - 2.988 \times 10^6 / (t +$   
470  $273.15)^2$  (Bottinga 1968;  $t = 180^\circ\text{C}$ ). Similarly, the  $\delta^{18}\text{O}_{\text{H}_2\text{O}}$  values that vary  
471 from  $+2.3$  to  $+4.0\text{‰}$  were calculated by using the function of  $1000\ln\alpha_{(\text{Calcite-H}_2\text{O})}$   
472  $= 2.78 \times 10^6 / (t + 273.15)^2 - 3.39$  (O'Neil et al. 1969;  $t = 180^\circ\text{C}$ ).

473 As shown in Figure 11, the proposed  $\delta^{13}\text{C}_{\text{fluid}}$  values ( $-4.2$ - $+0.4\text{‰}$ ) are higher  
474 than those of the mantle and sedimentary organic matter, but are similar to  
475 those of both fresh limestone and typical marine carbonate rocks. However,  
476 the calculated  $\delta^{18}\text{O}_{\text{fluid}}$  values ( $+2.3$ - $+4.0\text{‰}$ ) are different from the above three  
477 geological reservoirs, but overlap with those of metamorphic water ( $+2$ - $+25\text{‰}$ ;  
478 Hoefs 2009). Therefore, the theoretical  $\delta^{13}\text{C}_{\text{fluid}}$  and  $\delta^{18}\text{O}_{\text{fluid}}$  values suggest  
479 that the source of C is the main  $^{13}\text{C}$ -enriched limestone, while O is from a  
480 mixed source of  $^{18}\text{O}$ -depleted metamorphic water and  $^{18}\text{O}$ -enriched limestone.  
481 As suggested by in situ S and Pb isotopic evidence (Figs. 14-18), the  
482 ore-hosting sedimentary rocks and underlying metamorphic rocks are the two  
483 principal sources of mineralizing elements and associated fluids for the  
484 Nayongzhi deposit (see below).

485 (ii) Mechanism of calcite precipitation

486 Because the solubility of calcite decreases with increasing of temperature (e.g.,  
487 [Zheng 1990](#); [Barnes 1997](#)), cooling of hydrothermal fluids themselves could  
488 not result in calcite precipitation. In an open hydrothermal system, the major  
489 mechanism that can cause calcite precipitation include fluid mixing, water/rock  
490 (W/R) interaction and CO<sub>2</sub> degassing (e.g., [Zheng 1990](#); [Zheng and Hoefs](#)  
491 [1993](#); [Hoefs 2009](#); [Du et al. 2017](#)). The high and uniform C isotopic  
492 composition of syn-ore calcite suggests a main limestone source for C ([Fig. 11](#)),  
493 and so the fluid mixing cannot be the dominant mechanism resulting in calcite  
494 precipitation. The W/R interaction can generate a circulating process between  
495 dissolution and re-crystallization of local carbonate (e.g., [Warren 2000](#)). Such  
496 a circulating process of carbonate precipitation → dissolution →  
497 re-precipitation produced the metastable physical-chemical condition that is  
498 requested for giant sulfide mineralization and contributed to calcite  
499 precipitation. Further, using C and O isotope fractionation factors and  
500 equations (e.g., [O'Neil et al. 1969](#); [Zheng and Hoefs 1993](#)), we simulated the C  
501 and O isotopic evolution curves of calcite precipitated by the interaction  
502 between supposed metamorphic fluids ( $\delta^{13}\text{C}_{\text{fluid}} = -2\text{‰}$ ,  $\delta^{18}\text{O}_{\text{fluid}} = +6\text{‰}$ ) and  
503 carbonate rocks ([Fig. 12](#)). The simulation result suggests that our C and O  
504 isotopic data match well with the evolution curve of HCO<sub>3</sub><sup>-</sup> as the dominant C  
505 species ([Fig. 12](#); [Zheng and Hoefs 1993](#)). Similarly, the C and O isotopic  
506 compositions of calcite precipitated by CO<sub>2</sub> degassing (with 0.1, 0.2, 0.3 and

507 0.4 mol fraction of total C and O;  $\delta^{13}\text{C}_{\text{fluid}} = -2\text{‰}$ ,  $\delta^{18}\text{O}_{\text{fluid}} = +6\text{‰}$ ) were  
508 simulated (Fig. 13A-B). The result shows that our C and O isotopic data still  
509 match well with the evolution curve of  $\text{HCO}_3^-$  as the dominant C species (Fig.  
510 13B). We thus propose that both the W/R interaction and  $\text{CO}_2$  degassing are  
511 the main mechanisms for calcite precipitation in the Nayongzhi deposit.

512 (II) Source of S, formation mechanism, and isotope fractionation

513 (i) Source of S

514 The fact that both in situ S isotopic data ( $\delta^{34}\text{S} = +11.8\text{--}+33.0\text{‰}$ ) and the bulk  
515 ones ( $\delta^{34}\text{S} = +17.17\text{--}+24.79\text{‰}$ ) (Table 3) reflect the enrichment of  $^{34}\text{S}$  in  
516 hydrothermal fluids, a typical characteristic of marine sulfate-derived S. In  
517 addition, it has been well-documented that  $\delta^{34}\text{S}_{\text{barite}} > \delta^{34}\text{S}_{\text{fluid}} > \delta^{34}\text{S}_{\text{sulfide}}$  if  
518 the hydrothermal minerals contain barite (e.g., Ohmoto 1972; Ohmoto et al.  
519 1990). Thus, the  $\delta^{34}\text{S}_{\text{fluid}}$  value should be higher than the minimum or average  
520  $\delta^{34}\text{S}_{\text{sulfide}}$  value determined by in situ and bulk analyses (Figs. 14-15) as  
521 recorded by the paragenetic association of barite in post-ore phase (Table 1;  
522 Peng et al. 2016), i.e.  $\delta^{34}\text{S}_{\text{fluid}} > +11.8$  or  $+17.17\text{‰}$  (minimum in situ and bulk  
523  $\delta^{34}\text{S}_{\text{sulfide}}$  values, respectively) or  $+21.7\text{‰}$  (mean value of all measured data).  
524 Such S isotopic signatures differ from mantle-derived S ( $0 \pm 3\text{‰}$ : Chaussidon  
525 et al. 1989), but overlap with those of the sulfate-bearing (barite/gypsum)  
526 evaporates within Cambrian to Triassic marine sedimentary strata in the  
527 studied region (Fig. 14B;  $\delta^{34}\text{S} = +22\text{--}+28\text{‰}$ : Jin 2008; Zhou et al. 2013a) and  
528 the Ediacaran to Cambrian seawater (Fig. 14A-B;  $\delta^{34}\text{S} = +25\text{--}+35\text{‰}$ : Claypool



529 [et al. 1980](#); [Seal 2006](#)). As  $\Delta^{34}\text{S}_{\text{sulfate-sulfide}}$  can be high up to +15‰ in the  
530 process of thermochemical sulfate reduction ([Ohmoto et al. 1990](#); [Machel et al.](#)  
531 [1995](#); [Worden et al. 1995](#); [Ohmoto and Goldhaber 1997](#)), so the theoretical  
532  $\delta^{34}\text{S}_{\text{sulfide}}$  value could down to +7‰ or +10‰, if the reduced S was completely  
533 derived from evaporates or seawater. The theoretically predicted  $\delta^{34}\text{S}_{\text{sulfide}}$   
534 values sourced from both of the above two reservoirs can match well with the  
535 observed  $\delta^{34}\text{S}$  values (> +11.8‰; [Fig. 14C](#)). This suggests multiple S  
536 reservoirs for  $\text{S}^{2-}$  in the studied deposit. Previous studies showed that the S in  
537 the nearby carbonate-hosted Zn-Pb deposits, such as Shaojiwan (hosts in  
538 Permian), Tianqiao, Qingshan and Shanshulin (hosts in Carboniferous) ([Figs.](#)  
539 [2, 14A-B](#)), is also derived from multiple S reservoirs ([Zhou et al. 2013a, 2014b](#);  
540 [Li et al., 2015](#)).

541 (ii) Formation mechanism of reduced S

542 Two mechanisms, including bacterial sulfate reduction (BSR) and  
543 thermochemical sulfate reduction (TSR), have been employed to explain the  
544 formation of  $\text{S}^{2-}$  from  $\text{SO}_4^{2-}$  (e.g., [Seal 2006](#); [Basuki et al. 2008](#); [Zhou et al.](#)  
545 [2014a](#)). These two reduction processes are temperature-dependent. BSR  
546 occurs at a relatively low T (< 110°C: [Jørgenson et al. 1992](#); [Basuki et al. 2008](#)).  
547 The homogenization temperature of fluid inclusions in quartz (113-232°C; [Zhu](#)  
548 [et al. 2016](#)) is too high for bacteria to survive. So BSR played an insignificant  
549 role in the formation of  $\text{S}^{2-}$ . TSR occurs at a relatively high T (> 100-140°C:  
550 [Machel et al. 1995](#); [Worden et al. 1995](#)) and can produce a large amount of  $\text{S}^{2-}$ ,

551 with relatively stable  $\delta^{34}\text{S}$  values (e.g., [Ohmoto et al. 1990](#); [Seal 2006](#)).  
552 Moreover, the mixed process of hot and cold ore-forming fluids could form  $\text{S}^{2-}$   
553 from  $\text{SO}_4^{2-}$  by TSR through the reactions of  $\text{SO}_4^{2-} + 2\text{C} = \text{S}^{2-} + 2\text{CO}_2$ ,  $\text{SO}_4^{2-} +$   
554  $\text{CH}_4 = \text{H}_2\text{S} + \text{CO}_3^{2-} + \text{H}_2\text{O}$  or  $\text{SO}_4^{2-} + 2\text{CH}_2\text{O} = \text{H}_2\text{S} + \text{HCO}_3^-$  (e.g., [Worden et al.](#)  
555 [1995](#); [Leach et al., 2005](#)). We thus propose that the TSR has played a key role  
556 in the formation of  $\text{S}^{2-}$  in the Nayongzhi deposit.

557 (iii) S isotope fractionation

558 The similarity of bulk S isotopic composition between pyrite ( $\delta^{34}\text{S} =$   
559  $+18.12\text{--}+22.06\text{‰}$ ) and sphalerite ( $\delta^{34}\text{S} = +17.17\text{--}+24.79\text{‰}$ ) precipitated at  
560 different ore-forming stages ([Table 2](#); [Fig. 14C](#)) indicates that the bulk S  
561 isotopic data could not reflect the real S isotope fractionation. The disparity of in  
562 situ  $\delta^{34}\text{S}$  values between pyrite ( $+15.1\text{--}+27.0\text{‰}$ ) and sphalerite ( $+11.8\text{--}+33.0\text{‰}$ )  
563 crystals suggests that in situ determined S isotopes can reflect the nature of  
564 fractionation involved in mineralization. As shown in [Figure 15A](#), rims of pyrite  
565 crystal have  $\delta^{34}\text{S}$  values ( $+15.1\text{--}+15.3\text{‰}$ ) higher than those of rims of  
566 paragenetic sphalerite crystal ( $\delta^{34}\text{S} = +11.8\text{--}+11.9\text{‰}$ ). Such S isotopic  
567 signatures suggest that S isotope fractionation between pyrite and paragenetic  
568 sphalerite has reached thermodynamic equilibrium (e.g. [Ohmoto et al. 1990](#);  
569 [Seal 2006](#)). We thus propose an equilibrium S isotope fractionation between  
570 paragenetic sulfide minerals, at least locally.

571 In addition, the in situ S isotopic ratios decrease from the core to rim of both  
572 pyrite and sphalerite crystals ([Fig. 15A](#)), which can be explained by (a)

573 variation of physical-chemical condition (T, pH,  $f_{O_2}$ , etc.) in single S reservoir  
574 (Seal 2006); (b) mixture of multiple S reservoirs (Ohmoto et al. 1990); or (c)  
575 dynamic fractionation of S isotopes (Hoefs 2009). Previous studies suggested  
576 that the change of physical-chemical condition can cause significant variation  
577 of S isotopes in hydrothermal system (e.g., Seal 2006; Hoefs 2009). However,  
578 the circulating process of carbonate dissolution → re-precipitation can provide  
579 a metastable environment for giant mineralization (see above), so the variation  
580 of physical-chemical condition is indistinctive, and thus plays an insignificant  
581 role in the decreasing  $\delta^{34}\text{S}$  values from core to rim of sulfide crystals. The  
582 mixed process of the heavy S isotope-enriched fluid and the  $^{34}\text{S}$ -depleted fluid  
583 can cause significant variation of S isotopes (e.g., Seal 2006). Both bulk and in  
584 situ S isotopic data in this study suggests multiple S reservoirs for  $\text{S}^{2-}$  in the  
585 Nayongzhi deposit, so the observed decrease of S isotopes from core to rim of  
586 sulfide crystals (Fig. 15A) may be the result of a mixture of multiple S  
587 reservoirs. Alternatively, the rapid precipitation of sulfide minerals can cause a  
588 strong Rayleigh fractionation of S isotopes during the process of fluid mixing.  
589 As a consequence of the dynamic fractionation,  $^{34}\text{S}$  is expected to be more  
590 enriched in the core of sulfide crystals than their rim (Fig. 15A).

### 591 (III) Source of ore-forming metal

592 Because of extremely low contents of U and Th in sulfide minerals (especially  
593 galena), time-integrated effect of U and Th on radiogenic Pb isotopes in  
594 sulfides is negligible (e.g., Carr et al, 1995; Muechez et al. 2005; Pass et al.

595 [2014; Zhou et al. 2014b](#)). Therefore, the Pb isotopic ratios of galena from the  
596 Nayongzhi deposit can represent those of hydrothermal fluids. The narrow  
597 range of in situ Pb isotopic data suggests a single source or else a well-mixed  
598 source of Pb ([Table 4; Fig. 16A-B](#)). In the plot of  $^{207}\text{Pb}/^{204}\text{Pb}$  vs.  $^{206}\text{Pb}/^{204}\text{Pb}$   
599 ([Fig. 16A](#)), all the Pb isotopic data plot in the field that overlaps with the Pb  
600 evolution curve of the upper crust contributed to the orogeny and the field of  
601 modern lower crust ([Zartman and Doe 1981](#)). Similarly, in the  $^{208}\text{Pb}/^{204}\text{Pb}$  vs.  
602  $^{206}\text{Pb}/^{204}\text{Pb}$  diagram ([Fig. 16B](#)), all the Pb isotopic data also plot into the field of  
603 modern lower crust ([Zartman and Doe 1981](#)). This suggests that the source of  
604 Pb is the deep continental crust (e.g., [Zartman and Doe 1981](#)). Again, the  $\mu$   
605 values ( $^{238}\text{U}/^{204}\text{Pb} = 9.64\text{-}9.67$ ) of the galena are slightly higher than that of the  
606 mean value of the continental crust ( $\mu = 9.58$ ), also indicating a deep-seated  
607 crustal source for Pb (e.g., [Carr et al. 1995](#)).

608 As shown in [Figure 16A](#), at a given  $^{207}\text{Pb}/^{204}\text{Pb}$  ratio, the galena displays  
609 significantly lower  $^{206}\text{Pb}/^{204}\text{Pb}$  ratios than those of the Permian Emeishan flood  
610 basalts, and Ediacaran carbonate rocks. Such Pb isotopic signatures rule out  
611 the main contribution of Pb metal from mantle-derived magmatic rocks and  
612 ore-hosting sedimentary rocks. On the contrary, in situ Pb isotopic ratios of the  
613 galena are similar to those of the Proterozoic metamorphic rocks ([Fig. 16A](#)).

614 This further suggests a continental crustal origin for Pb in hydrothermal fluids  
615 and the basement rocks provided the majority of Pb metal.

616 The in situ Pb isotopic ratios gradually increase from galena-I (fine-grained) to

617 galena-II (coarse-grained) in both  $^{207}\text{Pb}/^{204}\text{Pb}$  vs.  $^{206}\text{Pb}/^{204}\text{Pb}$  (Fig. 17A) and  
618  $^{208}\text{Pb}/^{204}\text{Pb}$  vs.  $^{206}\text{Pb}/^{204}\text{Pb}$  diagrams (Fig. 17B). There are two possibilities: (i)  
619 U and Th contents of galena-II are relatively higher than those of galena-I; or (ii)  
620 high radiogenic Pb-enriched source provides more Pb for galena-II than  
621 galena-I. Trace elements determined by LA-ICPMS show that there is no  
622 significant difference of both U and Th contents between two generations of  
623 galena (Ye Lin et al. 2011 and unpublished data). Furthermore, Pb isotopic  
624 data of galena-I overlap with those of galena-II in the diagram of  $^{208}\text{Pb}/^{206}\text{Pb}$  vs.  
625  $^{207}\text{Pb}/^{206}\text{Pb}$  (Fig. 18), suggesting that both of them have the same contents of  
626 U and Th. On the contrary, in both  $^{207}\text{Pb}/^{204}\text{Pb}$  vs.  $^{206}\text{Pb}/^{204}\text{Pb}$  (Fig. 17A),  
627  $^{208}\text{Pb}/^{204}\text{Pb}$  vs.  $^{206}\text{Pb}/^{204}\text{Pb}$  (Fig. 17B), and  $^{208}\text{Pb}/^{206}\text{Pb}$  vs.  $^{207}\text{Pb}/^{206}\text{Pb}$   
628 diagrams (Fig. 18), the Pb isotopic compositions of two generations of galena  
629 form two distinct evolution curves. This implies that the high radiogenic  
630 Pb-enriched source (most likely the ore-hosting sedimentary rocks) provides  
631 more Pb for the ore-forming fluids at the late phase than the early phase, and  
632 thus slightly changes the evolution curve of Pb isotopes.

### 633 **Timing of mineralization**

634 The occurrence of ore body (Fig. 6) and sulfide ore (Figs. 7-8), and the  
635 evidence of mineralogy (Figs. 9-10) and isotope geochemistry (Figs. 11-18)  
636 show that the Nayongzhi deposit belongs to epigenetic type. This means that  
637 the formation of the Nayongzhi deposit should posterior to the ore-hosting late  
638 Ediacaran and early Cambrian strata. In addition, the Nayongzhi deposit is

639 located at the northern margin of the Triassic Youjiang Basin and is structurally  
640 controlled by the Wuzhishan fold-fault system (Figs. 2-4), all of which were  
641 active during the Yanshanian Orogeny (e.g., [Chen et al. 2015](#)). Such an  
642 ore-controlling structure feature suggests that the Nayongzhi deposit was most  
643 likely formed in the Yanshanian period. Moreover, isotope geochronology  
644 studies suggest that the ages of carbonate-hosted Zn-Pb deposits in the SYG  
645 province are 226-165 Ma (e.g., [Mao et al. 2012](#); [Zhou et al. 2013a](#); [Zhang et al.](#)  
646 [2015](#)). Therefore, we propose that the Nayongzhi deposit formed in the early  
647 Yanshanian (late Triassic) and related to the evolution of the Triassic Youjiang  
648 Basin, and was most likely to be the product of basin-orogeny coupling.

649

650

## IMPLICATIONS

### 651 **Ore genesis type**

652 Ore body in the Nayongzhi deposit occurs as stratiform or lentiform (Figs. 6A-B,  
653 7A), with a clear strata-bound feature. This led some researchers to classify it  
654 as a SEDEX-type or sedimentation reworking type (e.g., [Chen et al. 2015](#); [Jin](#)  
655 [et al. 2015](#)). In fact, with the exception of stratiform or lentiform Zn-Pb ore body,  
656 the steeply dipping veined one is also developed (Figs. 6A, 7E). Furthermore,  
657 the ore-hosting rocks are late Ediacaran and early Cambria carbonate rocks,  
658 which differ from the siliciclastic rocks that host sulfide ore of the SEDEX-type  
659 (e.g., [Leach et al. 2005, 2010](#)). The newly-obtained bulk C-O and S isotopes,  
660 and in situ S and Pb isotopes, together with ore deposit geology and

661 mineralogy, suggesting an epigenetic origin for the Nayongzhi deposit.  
662 Extensive studies have suggested that the carbonate-hosted Zn-Pb deposits in  
663 the SYG province are epigenetic SYG-type and are characterized by: (a) ore  
664 body has a closely spatial association with the Emeishan mafic magmatism  
665 (Fig. 1B); (b) sulfide ore has a high grade, i.e. > 10 wt. % Zn + Pb, and rich in  
666 Ag, Cu, Cd, Ge and Ga (e.g., Ye et al. 2011; Zhou et al. 2013a; Zhu et al. 2017);  
667 (c) ore-forming fluids having low-medium temperature (120-280°C) and low  
668 salinity (2-10 wt. % NaCl equiv.) (e.g., Li et al. 2007; Zhou et al. 2014a; Zhu et  
669 al. 2016); and (d) a mixed metal source of overlying basalts, ore-hosting  
670 sedimentary rocks and underlying metamorphic rocks (e.g., Huang et al. 2010;  
671 Zhou et al. 2014b; Li et al. 2015, 2016). However, the Nayongzhi deposit is  
672 distinct from the nearby Zn-Pb deposits (Table 5) in: (a) ore body has no  
673 directly genetic association with igneous activity (Fig. 4); (b) sulfide ore  
674 having low ore grade, namely average 8-10 wt. % Zn + Pb; (c) ore-forming  
675 fluids are characterized by low temperature (113-232°C) and moderate salinity  
676 (10-15 wt. % NaCl equiv.) (Zhu et al. 2016); (d) basement-derived metals are  
677 dominant in hydrothermal fluids (Fig. 16A); and (e) carbonate solution collapse  
678 breccia is well-developed (Figs. 7-8). These mineralized features of the  
679 Nayongzhi deposit can be compared to those of typical MVT deposits (e.g.,  
680 Leach et al. 2005, 2010). So we interpret the Nayongzhi deposit to be an  
681 epigenetic MVT deposit.

## 682 **Ore formation process**

683 Through integrating all the information, this paper proposes a new working  
684 model to explain the Zn-Pb mineralization in the Wuzhishan anticline area (Fig.  
685 19) as follows: The basement-derived metal-bearing metamorphic fluids (as  
686 suggested by C-O and Pb isotopes; Figs. 12-13, 16-18) were driven upward  
687 along the regional Yadu-Ziyun fault (Figs. 2-3) by the late Indosinian Orogeny  
688 (226-205 Ma) and Triassic Youjiang Basing (e.g., Zhou et al. 2013a; Zhang  
689 et al. 2015), and then released into secondary structural units (such as the  
690 Wuzhishan anticline; Figs. 2-3) when the tectonic regimes shift from  
691 compression to extension at the early Yanshanian period (205-165 Ma) (e.g.,  
692 Qiu et al. 2016). These fluids were trapped into the platform carbonate  
693 sequences, where the evaporitic salt structure and sedimentary organic matter  
694 are well-developed (Fig. 19). This process resulted in the formation of  $S^{2-}$  from  
695  $SO_4^{2-}$  by TSR and the extraction of parts of mineralizing elements from the  
696 ore-hosting strata via the W/R interaction (as evidenced by C-O, S and Pb  
697 isotopes; Figs. 12-18). The rapid sulfide precipitation caused by mixing  
698 multiple S reservoirs with associated fluids results in significant fractionation of  
699 S isotopes (Figs. 14A-C, 15A). During the ore formation process, local  
700 carbonate acted as a buffer through repeated dissolution and re-precipitation,  
701 providing the metastable metallogenic environment for massive sulfide  
702 mineralization. According to our new model, some potential and buried ore  
703 bodies may be found in the future (Fig. 19).

704 From the above, this study implies that the extensional setting (Youjiang Basin)



705 facilitated the excretion of hydrothermal fluids, the fold structure (Wuzhishan  
706 anticline) was beneficial to trap fluids, the carbonate platform sequences  
707 supplied an S source and organic reducers, and the fluids then mixed and the  
708 carbonate buffer caused rapid and continued precipitation of sulfide minerals,  
709 all of which are crucial for the formation and exploration of MVT deposits in  
710 general.

711

712

### **ACKNOWLEDGEMENTS**

713 We thank Prof. Lin Ye and Prof. Rui-Zhong Hu (IGCAS), and Prof. David Leach  
714 (U.S. Geological Survey) for fruitful discussions. Prof. Fang-Zhen Teng  
715 (Associate Editor), Prof. Ben-Xun Su, and anonymous reviewers are also  
716 thanked for their constructive suggestions and comments. This research was  
717 financially supported by the Key Project of National Natural Science  
718 Foundation of China (41430315), the National Basic Research Program of  
719 China (2014CB440905), the Visiting Scholar Project of China Scholarship  
720 Council to Jia-Xi Zhou (201604910455), and ARC Future Fellowship (No.  
721 FT140100826) to Xuan-Ce Wang.

722

723

### **REFERENCES CITED**

724 Bai, J., Huang, Z., Zhu, D., Yan, Z., and Zhou, J. (2013) Isotopic compositions  
725 of sulfur in the Jinshachang lead-zinc deposit, Yunnan, China, and its  
726 implication on the formation of sulfur-bearing minerals. *Acta Geologica*

- 727 Sinica (English Edition), 87, 1355–1369.
- 728 Bao, Z., Yuan, W., Yuan, H., Liu, X., Chen, K., and Zong, C. (2016)  
729 Non-matrix-matched determination of lead isotope ratios in ancient bronze  
730 artifacts by femtosecond laser ablation multi-collector inductively coupled  
731 plasma mass spectrometry. International Journal of Mass Spectrometry,  
732 402, 12–19.
- 733 Barnes, H.L. (1997) Geochemistry of hydrothermal ore deposits. John Wiley &  
734 Sons, v. 1.
- 735 Barker, S.L., Hickey, K.A., Cline, J.S., Dipple, G.M., Kilburn, M.R., Vaughan,  
736 J.R., and Longo, A.A. (2009) Uncloaking invisible gold: Use of nanoSIMS  
737 to evaluate gold, trace elements, and sulfur isotopes in pyrite from  
738 Carlin-type gold deposits. Economic Geology, 104, 897–904.
- 739 Basuki, N.I., Taylor, B.E., and Spooner, E.T.C. (2008) Sulfur isotope evidence  
740 for thermo-chemical reduction of dissolved sulfate in Mississippi valley  
741 type zinc-lead mineralization, Bongara area, northern Peru. Economic  
742 Geology, 103, 183–799.
- 743 Bottinga, Y. (1968) Calculation of fractionation factors for carbon and oxygen  
744 isotopic exchange in the system calcite-carbon dioxide-water. The Journal  
745 of Physical Chemistry, 72, 800–808
- 746 Carr, G.R., Dean, J.A., Suppel, D.W., and Heithersay, P.S. (1995) Precise lead  
747 isotope fingerprinting of hydrothermal activity associated with Ordovician  
748 to Carboniferous metallogenic events in the Lachlan fold belt of New

- 749 South Wales. *Economic Geology*, 90, 1467–1505.
- 750 Carter, A., Roques, D., Bristow, C., and Kinny, P. (2001). Understanding  
751 Mesozoic accretion in Southeast Asia: significance of Triassic  
752 thermotectonism (Indosinian orogeny) in Vietnam. *Geology* 29, 211–214.
- 753 Chaussidon, M., Albarède, F., and Sheppard, S.M.F (1989) Sulphur isotope  
754 variations in the mantle from ion microprobe analyses of micro-sulphide  
755 inclusions. *Earth and Planetary Science Letters*, 92, 144–156.
- 756 Chen, G.Y., Wang, L., Fan, Y.M., and Zheng, W. (2015) Ore-search prospect of  
757 the deep subsurface in the Wuzhishan Pb-Zn ore field, Guizhou province.  
758 *Geology and Exploration*, 51, 859–869 (in Chinese with English abstract).
- 759 Chen, K.Y., Yuan, H.L., Bao, Z.A., Zong, C.L., and Dai, M.N. (2014) Precise  
760 and accurate in situ determination of lead isotope ratios in NIST, USGS,  
761 MPI-DING and CGSG glass reference materials using femtosecond laser  
762 ablation MC-ICP-MS. *Geostandards and Geoanalytical Research*, 38, 5–  
763 21.
- 764 Chen, M., Zhang, Z., Santosh, M., Dang, Y., and Zhang, W. (2015). The  
765 Carlin-type gold deposits of the “golden triangle” of SW China: Pb and S  
766 isotopic constraints for the ore genesis. *Journal of Asian Earth Sciences*,  
767 103, 115–128.
- 768 Claypool, G.E., Holser, W.T., Kaplan, I.R., Sakai, H., and Zak, I. (1980) The  
769 age curves of sulfur and oxygen isotopes in marine sulfate and their  
770 mutual interpretation. *Chemical Geology*, 28, 199–260.

- 771 Demény, A., Ahijado, A., Casillas, R., and Vennemann, T.W. (1998) Crustal  
772 contamination and fluid/rock interaction in the carbonatites of  
773 Fuerteventura (Canary Islands, Spain): A C, O, H isotope study. *Lithos*, 44,  
774 101–115.
- 775 Du, L.J., Li, B., Huang, Z.L., Zhou, J.X., Zou, G.F., and Yan, Z.F. (2017)  
776 Carbon-oxygen isotopic geochemistry of the Yangla Cu skarn deposit, SW  
777 China: Implications for the source and evolution of hydrothermal fluids.  
778 *Ore Geology Reviews*, 88, 809–821.
- 779 Friedman, I., and O'Neil, J.R. (1977) Compilation of stable isotope fractionation  
780 factors of geochemical interest. *Data of Geochemistry*, U.S. Geological  
781 Survey Professional Paper, 440-KK, p. 1–12.
- 782 Gao, S., Yang, J., Zhou, L., Li, M., Hu, Z.C., Guo, J.L., Yuan, H.L., Gong, H.J.,  
783 Xiao, G.Q., and Wei, J.Q. (2011) Age and growth of the Archean Kongling  
784 terrain, South China, with emphasis on 3.3 Ga granitoid gneisses.  
785 *American Journal of Sciences*, 311, 153–182.
- 786 Gustafson, L.B., and Williams, N. (1981) Sediment-hosted stratiform deposits  
787 of copper, lead and zinc. *Economic Geology*, 75, 139–178.
- 788 Heijlen, W., Muchez, P., Banks, D., Schneider, J., Kucha, H., and Keppens, E.  
789 (2003) Carbonate-hosted Zn-Pb deposits in Upper Silesia, Poland: Origin  
790 and Evolution of Mineralizing fluids and constraints on genetic models.  
791 *Economic Geology*, 98, 911–932.
- 792 Hoefs, J. (2009) *Stable isotope geochemistry* (sixth edition). Springer-Verlag

- 793 Berlin Heidelberg doi: 10.1007/978-3-540-70708-0
- 794 Hu, R.Z., and Zhou, M.F. (2012) Multiple Mesozoic mineralization events in  
795 South China-an introduction to the thematic issue. *Mineralium Deposita*,  
796 47, 579–588.
- 797 Hu, R., Fu, S., Huang, Y., Zhou, M., Fu, S., Zhao, C., Wang, Y., Bi, X., and Xiao,  
798 J. (2017) The giant South China Mesozoic low-temperature metallogenic  
799 domain: Reviews and a new geodynamic model. *Journal of Asian Earth*  
800 *Sciences*, 137, 9–34.
- 801 Huang, Z., Li, X., Zhou, M., Li, W., and Jin, Z. (2010) REE and C-O isotopic  
802 geochemistry of calcites from the world-class Huize Pb-Zn deposits,  
803 Yunnan, China: Implication for the ore genesis. *Acta Geologica Sinica*  
804 (English edition), 84, 597–613.
- 805 Ikehata, K., Notsu, K., and Hirata, T. (2008) In situ determination of Cu isotope  
806 ratios in copper-rich materials by NIR femtosecond LA-MC-ICPMS.  
807 *Journal of Analytical Atomic Spectrometry*, 23, 1003–1008.
- 808 Jian, P., Li, D.Y., Kröner, A., Zhang, Q., Wang, Y.Z., Sun, X.M., and Zhang, W.  
809 (2009) Devonian to Permian plate tectonic cycle of the Paleo-Tethys  
810 Orogen in southwest China (II): Insights from zircon ages of ophiolites,  
811 arc/back-arc assemblages and within-plate igneous rocks and generation  
812 of the Emeishan CFB province. *Lithos*, 113, 767–784.
- 813 Jin, C.H., Li, K., Huang, L., Zhang, Y., and Shen, Z.W. (2015) Characteristics of  
814 sulfur and lead isotope composition and metallogenic material source of

- 815 the Nayongzhi Pb-Zn deposit, northwestern Guizhou province. *Journal of*  
816 *Mineralogy and Petrology*, 35, 81–88 (in Chinese with English abstract).
- 817 Jin, Z.G. (2008) The ore-control factors, ore-forming regularity and ore  
818 forecasting of Pb-Zn deposits in NW Guizhou province. Engine Industry  
819 Press, Beijing, pp. 1–105 (in Chinese).
- 820 Jin, Z.G., Zhou, J.X., Huang, Z.L., Luo, K., Gao, J.G., Peng, S., Wang, B., and  
821 Chen, X.L. (2016). Ore genesis of the Nayongzhi Pb-Zn deposit, Puding  
822 city, Guizhou Province, China: Evidences from S and in situ Pb isotopes.  
823 *Acta Petrologica Sinica*, 32, 3441–3455.
- 824 Jørgenson, B.B., Isaksen, M.F., and Jannasch, H.W. (1992) Bacterial sulfate  
825 reduction above 100°C in deep sea hydrothermal vent sediments.  
826 *Science*, 258, 1756–1757.
- 827 Wilkinson, J.J., Stoffell, B., Wilkinson, C.C., Jeffries, T.E., and Appold, M.S.  
828 (2009) Anomalously metal-rich fluids form hydrothermal ore deposits.  
829 *Science*, 323, 764–767.
- 830 Leach, D.L., Bradley, D.C., Huston, D., Pisarevsky, S.A., Taylor, R.D., and  
831 Gardoll, S.J. (2010) Sediment-hosted lead-zinc deposits in Earth history.  
832 *Economic Geology*, 105, 593–625.
- 833 Leach, D.L., Sangster, D., Kelley, K.D., Large, R.R., Garven, G., Allen, C.,  
834 Gutzmer, J., and Walters, S. (2005) Sediment-hosted lead-zinc deposits:  
835 A global perspective. *Economic Geology*, 100<sup>th</sup> Ann 561–607.
- 836 Li, B., Zhou, J.X., Huang, Z.L., Yan, Z.F., Bao, G.P., and Sun, H.R. (2015)

- 837 Geological, rare earth elemental and isotopic constraints on the origin of  
838 the Banbanqiao Zn-Pb deposit, southwest China. *Journal of Asian Earth*  
839 *Sciences*, 111, 100–112.
- 840 Li, B., Zhou, J., Li, Y., Chen, A., and Wang, R. (2016) *Geology and Isotope*  
841 *Geochemistry of the Yinchanggou-Qiluogou Pb-Zn Deposit, Sichuan*  
842 *Province, Southwest China. Acta Geologica Sinica (English Edition)*, 90,  
843 1768–1779.
- 844 Li, W.B., Huang, Z.L., and Yin, M.D. (2007) Dating of the giant Huize Zn-Pb ore  
845 field of Yunnan province, southwest China: Constraints from the Sm-Nd  
846 system in hydrothermal calcite. *Resource Geology*, 57, 90–97.
- 847 Liao, W. (1984) Mineralization model and the characters of isotope  
848 composition of S and Pb in the Pb-Zn metallic area in the East and West  
849 Yunnan Province, China. *Geology and Prospecting*, 1, 1–6 (in Chinese  
850 with English abstract).
- 851 Lin, Z.Y., Wang, D.H., and Zhang, C.Q. (2010) Rb-Sr isotopic age of sphalerite  
852 from the Paoma lead-zinc deposit in Sichuan Province and its implications.  
853 *Geology of China*, 37, 488–196 (in Chinese with English abstract).
- 854 Liu, H.C., and Lin, W.D. (1999) Study on the law of Pb-Zn-Ag ore deposit in  
855 northeast Yunnan, China. Kunming, Yunnan University Press, pp. 1–468  
856 (in Chinese).
- 857 Liu, Y., Hu, Z., Gao, S., Günther, D., Xu, J., Gao, C., and Chen, H. (2008) In  
858 situ analysis of major and trace elements of anhydrous minerals by

- 859 LA-ICP-MS without applying an internal standard. *Chemical Geology*, 257,  
860 34–43.
- 861 Mao, J.W., Zhou, Z.H., Feng, C.Y., Wang, Y.T., Zhang, C.Q., Peng, H.J., and  
862 Miao, Y. (2012) A preliminary study of the Triassic large-scale  
863 mineralization in China and its geodynamic setting. *Geology of China*, 39,  
864 1437–1471 (in Chinese with English abstract).
- 865 Machel, H.G., Krouse, H.R., and Sassen, R. (1995) Products and  
866 distinguishing criteria of bacterial and thermo-chemical sulfate reduction.  
867 *Applied Geochemistry*, 10, 373–389.
- 868 Muecher, P., Heijlen, W., Banks, D., Blundell, D., Boni, M., and Grandia, F.  
869 (2005) Extensional tectonics and the timing and formation of basin-hosted  
870 deposits in Europe. *Ore Geology Reviews*, 27, 241–267.
- 871 Ohmoto, H., and Goldhaber, M.B. (1997) Sulfur and carbon isotopes, in  
872 Barnes HL (Editor), *Geochemistry of hydrothermal ore deposits*, 3<sup>rd</sup> edition.  
873 Wiley, New York pp. 517–611
- 874 Ohmoto, H., Kaiser, C.J., and Geer, K.A. (1990) Systematic of sulfur isotopes  
875 in recent marine sediments and ancient sediment-hosted base metal  
876 deposits In H.K Herbert and S.E. Ho (Editors), *Stable isotopes and Fluid  
877 Processes in Mineralisation*. Geol Dep Univ Extens, University of Western  
878 Australia 23: 70–120
- 879 Ohmoto, H. (1972) Systematics of Sulfur and Carbon Isotopes in Hydrothermal  
880 Ore Deposits. *Economic Geolog*, 67, 551–579.



- 881 O'Neil, J.R., Clayton, R.N., and Mayeda, T.K. (1969) Oxygen isotope  
882 fractionation in divalent metal carbonates. *Journal of Chemical Physics*,  
883 51, 5547–5558.
- 884 Pass, H.E., Cookem, D.R., Davidson, G., Maas, R., Dipple, G., Rees, C.,  
885 Ferreira, L., Taylor, C., and Deyell, C.L. (2014) Isotope geochemistry of  
886 the northeast zone, Mount Polley alkalic Cu-Au-Ag porphyry deposit,  
887 British Columbia: A case for carbonate assimilation. *Economic Geology*,  
888 109, 859–890.
- 889 Peevler, J., Fayek, M., Misra, K.C., and Riciputi, L.R. (2003) Sulfur isotope  
890 microanalysis of sphalerite by SIMS: constraints on the genesis of  
891 Mississippi valley-type mineralization, from the Mascot-Jefferson City  
892 district, East Tennessee. *Journal of Geochemical Exploration*, 80, 277–  
893 296.
- 894 Peng, S., Jin, Z.G., Lin, G.S., Zhu, Y.Q., and Wang, B (2016) Analysis of  
895 ore-controlling factors and metallogenic model of Wuzhishan Pb-Zn  
896 deposit, Guizhou: A case study of Nayongzhi deposit. *Mineral Exploration*,  
897 7, 463–470 (in Chinese with English abstract).
- 898 Qiu, L., Tang, S.L., Wang, Q., Yang, W.X., Tang, X.L., and Wang, J.B. (2016)  
899 Mesozoic geology of southwestern China: Indosinian foreland  
900 overthrusting and subsequent deformation. *Journal of Asian Earth  
901 Sciences*, 122, 91–105.
- 902 Qiu, Y.M., Gao, S., McNaughton, N.J., Groves, D.I., and Ling, W.L. (2000) First

- 903 evidence of >3.2 Ga continental crust in the Yangtze craton of south China  
904 and its implications for Archean crustal evolution and Phanerozoic  
905 tectonics. *Geology*, 28, 11–14.
- 906 Reid, A., Wilson, C.J.L., Shun, L., Pearson, N., and Belousova, E. (2007)  
907 Mesozoic plutons of the Yidun Arc, SW China: U-Pb geochronology and  
908 Hf isotopic signature. *Ore Geology Reviews*, 31, 88–106.
- 909 Steinhoefel, G., Horn, I., and von Blanckenburg, F. (2009) Micro-scale tracing  
910 of Fe and Si isotope signatures in banded iron formation using  
911 femtosecond laser ablation. *Geochimica et Cosmochimica Acta*, 73,  
912 5343–5360.
- 913 Seal, I.R. (2006) Sulfur isotope geochemistry of sulfide minerals. *Review of*  
914 *Mineralogy and Geochemistry*, 61, 633–677.
- 915 Taylor, H.P., Frechen, J., and Degens, E.T. (1967) Oxygen and carbon isotope  
916 studies of carbonatites from the Laacher See District, West Germany and  
917 the Alnö District, Sweden. *Geochimica et Cosmochimica Acta*, 31, 407–  
918 430.
- 919 Tu GZ (1984) *Geochemistry of Strata-bound Ore Deposits in China* (Volumes  
920 I). Science Press, Beijing, pp. 13–69 (in Chinese with English abstract)
- 921 Veizer, J., and Hoefs, J. (1976) The nature of  $O^{18}/O^{16}$  and  $C^{13}/C^{12}$  secular  
922 trends in sedimentary carbonate rocks. *Geochimica et Cosmochimica*  
923 *Acta*, 40, 1387–1395
- 924 Warren, J. (2000) Dolomite: occurrence, evolution and economically important

- 925 associations. *Earth Science-Review*, 52, 1–81.
- 926 Wang, C.M., Deng, J., Carranza, E.J.M., and Lei, X.R. (2014) Nature, diversity  
927 and temporal-spatial distributions of sediment-hosted Pb-Zn deposit in  
928 China. *Ore Geology Reviews*, 56, 327–351.
- 929 Wang, L.J. (1994) Geological and geochemical features of lead-zinc deposits  
930 in northwestern, Guizhou Province, China. *Journal of Guilin College of*  
931 *Geology*, 14, 125–130 (in Chinese with English abstract).
- 932 Wei, A.Y., Xue, C.D., Xiang, K., Li, J., Liao, C., and Akhter, Q.J. (2015) The  
933 ore-forming process of the Maoping Pb-Zn deposit, northeastern Yunnan,  
934 China: Constraints from cathodoluminescence (CL) petrography of  
935 hydrothermal dolomite. *Ore Geology Reviews*, 70, 562–577.
- 936 Wong, W.H. (1927) Crustal movements and igneous activities in eastern China  
937 since Mesozoic time. *Bulletin Geol Association China*, 6, 9–37.
- 938 Worden, R.H., Smalley, P.C., and Oxtoby, N.H. (1995) Gas souring by the  
939 thermo chemical sulfate reduction at 140°C. *AAPG Bulletin* 79, 854–863.
- 940 Xie, J.R. (1963) Introduction of the Chinese Ore Deposits. Scientific Books  
941 Publishing House, Beijing, pp. 1–71 (in Chinese).
- 942 Xu, Y., Huang, Z., Zhu, D., and Luo, T. (2014) Origin of hydrothermal deposits  
943 related to the Emeishan magmatism. *Ore Geology Reviews*, 63, 1–8.
- 944 Yan, D.P., Zhou, M.F., Song, H.L., Wang, X.W., and Malpas, J. (2003) Origin  
945 and tectonic significance of a Mesozoic multilayer overthrust system  
946 within the Yangtze Block (South China). *Tectonophysics*, 361, 239–254.

- 947 Yan, Z.F., Huang, Z.L., Xu, C., Chen, M., and Zhang, Z.L. (2007) Signatures of  
948 the source for the Emeishan flood basalts in the Ertan area: Pb isotope  
949 evidence. *Chinese Journal of Geochemistry*, 26, 207–213.
- 950 Ye, L., Cook, N.J., Ciobanu, C.L., Liu, Y.P., Zhang, Q., Liu, T.G., Gao, W., Yang,  
951 Y.L., and Danyushevsky, L. (2011) Trace and minor elements in sphalerite  
952 from base metal deposits in South China: a LA–ICPMS study. *Ore  
953 Geology Reviews*, 39, 188–217.
- 954 Yuan, H.L., Yin, C., Liu, X., Chen, K.Y., Bao, Z.A., Zong, C.L., Dai, M.N., Lai,  
955 S.C., Wang, R., and Jiang, S.Y. (2015) High precision in-situ Pb isotopic  
956 analysis of sulfide minerals by femtosecond laser ablation multi-collector  
957 inductively coupled plasma mass spectrometry. *Science China Earth  
958 Science*, 58, 1713–1721.
- 959 Zartman, R.E., and Doe, B.R. (1981) Plumbotectonics-the model.  
960 *Tectonophysics*, 75, 135–162.
- 961 Zaw, K., Peters, S.G., Cromie, P., Burrett, C., and Hou, Z.Q. (2007) Nature,  
962 diversity of deposit types and metallogenic relations of South China. *Ore  
963 Geology Reviews*, 31, 3–47.
- 964 Zhang, C., Wu, Y., Hou, L., and Mao, J. (2015) Geodynamic setting of  
965 mineralization of Mississippi Valley-type deposits in world-class  
966 Sichuan-Yunnan-Guizhou Zn-Pb triangle, southwest China: Implications  
967 from age-dating studies in the past decade and the Sm-Nd age of the  
968 Jinshachang deposit. *Journal of Asian Earth Sciences*, 103, 103–114.

- 969 Zhang, J., Lin, Y., Yang, W., Shen, W., Hao, J., Hu, S., and Cao, M. (2014)  
970 Improved precision and spatial resolution of sulfur isotope analysis using  
971 NanoSIMS. *Journal of Analytical Atomic Spectrometry*, 29, 1934–1943.
- 972 Zheng, M.H., and Wang, X.C. (1991) Genesis of the Daliangzi Pb-Zn deposit in  
973 Sichuan, China. *Economic Geology*, 86, 831–846.
- 974 Zheng, Y.F. (1990) Carbon-oxygen isotopic covariation in hydrothermal calcite  
975 during degassing of CO<sub>2</sub>. *Mineralium Deposita*, 25, 246–250.
- 976 Zheng, Y.F., and Hoefs, J. (1993) Carbon and oxygen isotopic covariations in  
977 hydrothermal calcites. *Mineralium Deposita*, 28, 79–89.
- 978 Zhou, C.X., Wei, C.S., and Guo, J.Y. (2001) The source of metals in the  
979 Qilingchang Pb-Zn deposit, Northeastern Yunnan, China: Pb-Sr isotope  
980 constraints. *Economic Geology*, 96, 583–598.
- 981 Zhou, J.X., Huang, Z.L., Lv, Z.C., Zhu, X.K., Gao, J.G., and Mirnejad, H.  
982 (2014b) Geology, isotope geochemistry and ore genesis of the Shanshulin  
983 carbonate-hosted Pb-Zn deposit, southwest China. *Ore Geology Reviews*,  
984 63, 209–225.
- 985 Zhou, J., Huang, Z., and Yan, Z. (2013b) The origin of the Maozu  
986 carbonate-hosted Pb-Zn deposit, southwest China: Constrained by  
987 C-O-S-Pb isotopic compositions and Sm-Nd isotopic age. *Journal of Asian  
988 Earth Sciences*, 73, 39–47.
- 989 Zhou, J., Huang, Z., Zhou, M., Li, X., and Jin, Z. (2013a) Constraints of  
990 C-O-S-Pb isotope compositions and Rb-Sr isotopic age on the origin of

- 991 the Tianqiao carbonate-hosted Pb-Zn deposit, SW China. *Ore Geology*  
992 *Reviews*, 53, 77–92.
- 993 Zhou, J.X., Huang, Z.L., Zhou, M.F., Zhu, X.K., and Muchez, P. (2014a) Zinc,  
994 sulfur and lead isotopic variations in carbonate-hosted Pb-Zn sulfide  
995 deposits, southwest China. *Ore Geology Reviews*, 58, 41–54.
- 996 Zhou, J.X., Bai, J.H., Huang, Z.L., Zhu, D., Yan, Z.F., and Lv, Z.C. (2015)  
997 Geology, isotope geochemistry and geochronology of the Jinshachang  
998 carbonate-hosted Pb-Zn deposit, southwest China. *Journal of Asian Earth*  
999 *Sciences*, 98, 272–284.
- 1000 Zhou, M.F., Yan, D.P., Kennedy, A.K., Li, Y.Q., and Ding, J. (2002) SHRIMP  
1001 zircon geochronological and geochemical evidence for Neo-Proterozoic  
1002 arc-related magmatism along the western margin of the Yangtze Block,  
1003 South China. *Earth and Planetary Science Letters*, 196, 1–67.
- 1004 Zhou, M.F., Zhao, X.F., Chen, W.T., Li, X.C., Wang, W., Yan, D.Y., and Qiu, H.N.  
1005 (2014c) Proterozoic Fe-Cu metallogeny and supercontinental cycles of  
1006 the southwestern Yangtze Block, southern China and northern Vietnam.  
1007 *Earth Science-Review*, 139, 59–82.
- 1008 Zhu, C.W., Wen, H.J., Zhang, Y.X., Fu, S.H., Fan, H.F., and Cloquet, C. (2017)  
1009 Cadmium isotope fractionation in the Fule Mississippi Valley-type deposit,  
1010 Southwest China. *Mineralium Deposita*, 52, 675–686.
- 1011 Zhu, L.Y., Su, W.C., Shen, N.P., Dong, S.D., Cai, J.L., Zhang, Z.W., Zhao, H.,  
1012 and Xie, P. (2016) Fluid inclusion and sulfur isotopic studies of lead-zinc

1013 deposits, northwestern Guizhou, China. *Acta Petrologica Sinica*, 32,  
1014 3431–3440 (in Chinese with English abstract).

1015

1016 Figure captions

1017 FIGURE 1. A: Regional geological setting of South China, highlighting the  
1018 general study area; B: Geological sketch map of the Sichuan-Yunnan-Guizhou  
1019 (SYG) Pb-Zn metallogenic province (modified from [Liu and Lin 1999](#) and [Yan  
1020 DP unpublished map](#)), which shows the distribution of Zn-Pb deposit, strata,  
1021 fault and Emeishan basalts.

1022

1023 FIGURE 2. Geological sketch map of the NW Guizhou Zn-Pb metallogenic  
1024 district (modified from [Zhou et al. 2013a](#)), which shows the distribution of  
1025 Zn-Pb deposit, strata, fault and mafic dykes.

1026

1027 FIGURE 3. Geological sketch map of the southeastern part of the NW Guizhou  
1028 district (modified from [Chen et al. 2015](#)), which displays the fault, strata,  
1029 ore-controlling structure, and Zn-Pb, Au, phosphate and fluorite deposits.

1030

1031 FIGURE 4. Geological sketch map of the Wuzhishan anticline area (modified  
1032 from [Peng et al. 2016](#)), which reveals the ore-controlling structure, strata and  
1033 Zn-Pb deposit.

1034

1035 FIGURE 5. A generalized stratigraphic map of the Nayongzhi mining area,  
1036 which shows the lithology of ore-hosting strata and location of Zn-Pb ore body.

1037

1038 FIGURE 6. A: Cross-section map of No. 17 exploration line (modified from  
1039 [Peng et al. 2016](#)); B: Cross-section map of No. 23 exploration line (modified  
1040 from [Chen et al. 2015](#)). Strata, lithology, ore body and fault are shown in both  
1041 maps.

1042

1043 FIGURE 7. The picture of sulfide ore and post-ore hydrothermal vein, which  
1044 shows the geometry feature of ore body and aggregate structural feature of  
1045 hydrothermal minerals. A: Stratiform and lentiform ore bodies; B: Sulfide and  
1046 carbonate mineral veins; C: Massive sulfide and two phases of calcite/dolomite;  
1047 D: Sulfide vein cements dolostone breccia; E: Steeply dipping veined ore body  
1048 occurs along F<sub>7</sub> reverse fault; F: Post-ore quartz and barite vein fills into  
1049 fracture of wall rocks; G: Sulfide vein fills and cements dolostone breccia; H:  
1050 Disseminated sphalerite and post-ore calcite/dolomite fills into fracture of wall  
1051 rocks; I: Post-ore calcite/dolomite vein fills and cements dolostone breccia; J;  
1052 Sulfide vein cements dolostone breccia; K: Massive sulfide and veined sulfide  
1053 cements dolostone breccia; L: Post-ore calcite/dolomite vein fills and cements  
1054 dolostone breccia; M: Sulfide vein fills into fracture of silicified dolostone; N:  
1055 Massive sulfide; O: Sulfide vine cements dolostone breccia and post-ore  
1056 calcite/dolomite vein fills into fracture of wall rocks; P: Post-ore barite vein fills



1057 into fracture of wall rocks.

1058

1059 FIGURE 8. The structural feature of sulfide ore in the Nayongzhi deposit. A-B:

1060 Sphalerite-I occurs as dense disseminated; C: Sphalerite-I occurs as dense

1061 disseminated and galena-I presents as sparse disseminated; D: Sphalerite-I

1062 and pyrite-I form massive ore; E: Sphalerite-II and galena-II form massive ore;

1063 F: Sphalerite-II, galena-II and pyrite-II form massive ore; G: Sphalerite-II

1064 presents as sparse disseminated and calcite-III vein fills into fracture of ore; H:

1065 Sphalerite-II vein cements dolostone breccia and calcite-III vein fills into

1066 fracture of ore; I: Sphalerite-I forms massive ore; J: Sphalerite-II vein cements

1067 dolostone breccia; K: Diagenetic pyrite in wall rocks; L: Sphalerite-II presents

1068 as disseminated or veined; M: Sphalerite-II replaces wall rocks and forms

1069 metasomatic vein; N: Sphalerite-II fills and cements carbonate breccia; O:

1070 Sphalerite-II fills into fracture of wall rocks; P: Sphalerite-II cements carbonate

1071 breccia.

1072

1073 FIGURE 9. The textural feature of hydrothermal minerals in the Nayongzhi

1074 deposit under microscope. A: Fine-grained calcite-I (Cal-I) is enclosed by

1075 sphalerite-I (Sp-I) that coexists with pyrite-I (Py-I), both of which are cemented

1076 by dolomite-II (dol-II); B: Sp-I is enclosed by Py-II that coexists with Sp-II and

1077 Dol-II; C: Sp-I and Py-I are cemented by Dol-II, Cal-III fills into the fracture; D:

1078 Quartz-I (Qtz-I) is enclosed by galena-II (Gn-II) that coexists with Sp-II, Dol-II

1079 and Qtz-II; E: Coarse-grained Sp-II coexists with or is cemented by Cal-II; F:  
1080 Sp-II coexists with Gn-II and Py-II, both of which are cemented by Dol-III; G:  
1081 Fine-grained Gn-I and veined Py-I and Sp-I are enclosed by Dol-II; H:  
1082 Fine-grained Py-I and Cal-I are enclosed by Sp-I that are replaced by Gn-II; L:  
1083 Diagenetic Py is cemented by Qtz; M: Py-I is replaced by Sp-II that coexists  
1084 with Cal-II; N: Coarse-grained Gn-II coexists with Sp-II and Cal-II; P:  
1085 Fine-grained Sp-I is enclosed by Gn-II that coexists with Sp-II and Cal-II.

1086

1087 FIGURE 10. The textural feature of hydrothermal minerals in the Nayongzhi  
1088 deposit under scanning electron microscope (SEM). A: Fine-grained  
1089 sphalerite-I (Sp-I) and pyrite-I (Py-I) are enclosed by galena-II (Gn-II) that is  
1090 cemented by dolomite-II (Dol-II); B: Sp-II coexists with Gn-II and Dol-II; C:  
1091 Paragenetic Sp-I, Gn-I, Py-I and Dol-I are enclosed by calcite-II (Cal-II); D:  
1092 Fine-grained Sp-I is enclosed by Py-II that coexists with Sp-II, Cal-II fills into  
1093 the fracture; E: Dol-I is enclosed by Cal-II that fills into the boundary of Sp-I  
1094 and Py-I; F: Sp-II replaces Py-I and coexists with Cal-II; G: Paragenetic Sp-II  
1095 and Gn-II are enclosed by Cal-II; H: Paragenetic Sp-II, Py-II and Gn-II are  
1096 enclosed by Cal-II; I: Py-II encloses Gn-I and coexists with Sp-II, both of which  
1097 are enclosed by Cal-II; J: Paragenetic Sp-I and Py-I are enclosed by Cal-II; K:  
1098 Fine-grained Gn-I and Dol-I are enclosed by Cal-II; Gn-II and Cal-II fill into the  
1099 fracture of sphalerite-I; L: Sp-II encloses fine granular Gn-I and coexists with  
1100 Gn-II and Cal-II; M: Paragenetic Sp-II, Gn-II and Cal-II; N: Cal-II cements Sp-II

1101 and Gn-II; O: Cal-II fills and cements Sp-II that contains Gn-I; P: Sp-II  
1102 encloses granular Py-I and coexists with Cal-II.

1103

1104 FIGURE 11. Plot of  $\delta^{13}\text{C}$  versus  $\delta^{18}\text{O}$  values. C-O isotopic data for mantle,  
1105 marine carbonate rocks and sedimentary organic matter are sourced from  
1106 [Taylor et al. \(1967\)](#), [Demény et al. \(1998\)](#), [Veizer and Hoefs \(1976\)](#) and [Hoefs](#)  
1107 [\(2009\)](#).

1108

1109 FIGURE 12. Plot of  $\delta^{13}\text{C}$  vs.  $\delta^{18}\text{O}$  for the calcite precipitated by W/R interaction  
1110 with variation of R/W ratio and temperature (400-50°C) for either  $\text{HCO}_3^-$  or  
1111  $\text{H}_2\text{CO}_3$  as the dominant dissolved C species (Zheng and Hoefs, 1993). Initial  
1112 metamorphic fluids:  $\delta^{13}\text{C} = -2\text{‰}$ ,  $\delta^{18}\text{O} = +6\text{‰}$ .  $\Delta = \delta_{\text{rock}}^i - \delta_{\text{rock}}^f$ ; I:  $\Delta^{13}\text{C} = +0.2\text{‰}$ ,  
1113  $\Delta^{18}\text{O} = +2\text{‰}$ ; II:  $\Delta^{13}\text{C} = +1\text{‰}$ ,  $\Delta^{18}\text{O} = +6\text{‰}$ ; III:  $\Delta^{13}\text{C} = +2\text{‰}$ ,  $\Delta^{18}\text{O} = +10\text{‰}$ .

1114

1115 FIGURE 13. Plots of  $\delta^{13}\text{C}$  vs.  $\delta^{18}\text{O}$  for calcite precipitated by  $\text{CO}_2$  degassing  
1116 with  $\text{H}_2\text{CO}_3$  (A) or  $\text{HCO}_3^-$  (B) as the dominant dissolved C species. The batch  
1117 (solid line) and Rayleigh (dashed line) degassing-precipitation models change  
1118 with temperature (400-50°C) and mol fraction of C in the degassed  $\text{CO}_2$  (0.1 to  
1119 0.4) (after Zheng, 1990). The  $\delta^{13}\text{C}$  and  $\delta^{18}\text{O}$  values of the initial ore-forming  
1120 fluids were taken as  $-2\text{‰}$  and  $+6\text{‰}$ , respectively.

1121

1122

1123 FIGURE 14. A: S isotopic composition for seawater sulfate, and the Nayongzhi  
1124 and nearby Zn-Pb deposits; B: S isotopic composition for the Nayongzhi  
1125 deposit and a brief comparison with the nearby Zn-Pb deposits,  
1126 sulfate-bearing evaporites, seawater and mantle-derived S; C: Histogram of  
1127 bulk and in situ S isotopic composition for the Nayongzhi deposit. S isotopic  
1128 data for the nearby Zn-Pb deposits and evaporites are taken from Jin (2008),  
1129 [Zhou et al \(2013a, 2014b\)](#) and [Li et al \(2015\)](#), for the mantle-derived S are  
1130 [taken from Chaussidon et al \(1989\)](#), for the seawater are taken from [Claypool](#)  
1131 [et al. \(1980\)](#) and [Seal \(2006\)](#).

1132

1133 FIGURE 15. A: In situ  $\delta^{34}\text{S}$  value in sphalerite and paragenetic pyrite crystals  
1134 from core to rim; B: The best target selected for in situ S isotope analysis that  
1135 has homogeneous isotopic composition (such as  $^{32}\text{S}$ ,  $^{34}\text{S}$ ,  $^{75}\text{As}$  and  $^{63}\text{Cu}^{32}\text{S}$ ).

1136

1137 FIGURE 16. Plots of  $^{207}\text{Pb}/^{204}\text{Pb}$  vs.  $^{206}\text{Pb}/^{204}\text{Pb}$  (A) and  $^{208}\text{Pb}/^{204}\text{Pb}$  vs.  
1138  $^{206}\text{Pb}/^{204}\text{Pb}$  (B) that present a brief comparison of the modern MORB, Pelagic  
1139 sediment, Oceanic islandvolcanic rocks, Upper Crust and Lower Crust Pb  
1140 ([Zartman and Doe 1981](#)), and whole-rock of Ediacaran carbonate rocks,  
1141 Permian Emeishan basalts and Proterozoic metamorphic rocks ([Li et al. 2007](#);  
1142 [Yan et al. 2007](#); [Zhou et al. 2013a, 2014a](#)). Solid lines enclose 80% of all data  
1143 points for each field, and dashed lines enclose probable average values.  
1144 Mantle (A), Orogeny (B), Upper crust contributed to the orogeny (C), and

1145 Lower crust contributed to the orogeny (D).

1146

1147 FIGURE 17. Plots of  $^{207}\text{Pb}/^{204}\text{Pb}$  vs.  $^{206}\text{Pb}/^{204}\text{Pb}$  (A) and  $^{208}\text{Pb}/^{204}\text{Pb}$  vs.  
1148  $^{206}\text{Pb}/^{204}\text{Pb}$  that reveal the variation in Pb isotopes from the early phase  
1149 galena-I to the late phase galena-II.

1150

1151 FIGURE 18. Diagram of  $^{208}\text{Pb}/^{206}\text{Pb}$  vs.  $^{207}\text{Pb}/^{206}\text{Pb}$  that shows the relationship  
1152 and evolution of two generations of galena.

1153

1154 FIGURE 19. An integrated working and ore exploration model of the  
1155 carbonate-hosted Zn-Pb deposits in the Wuzhishan anticline area.

Fig. 1

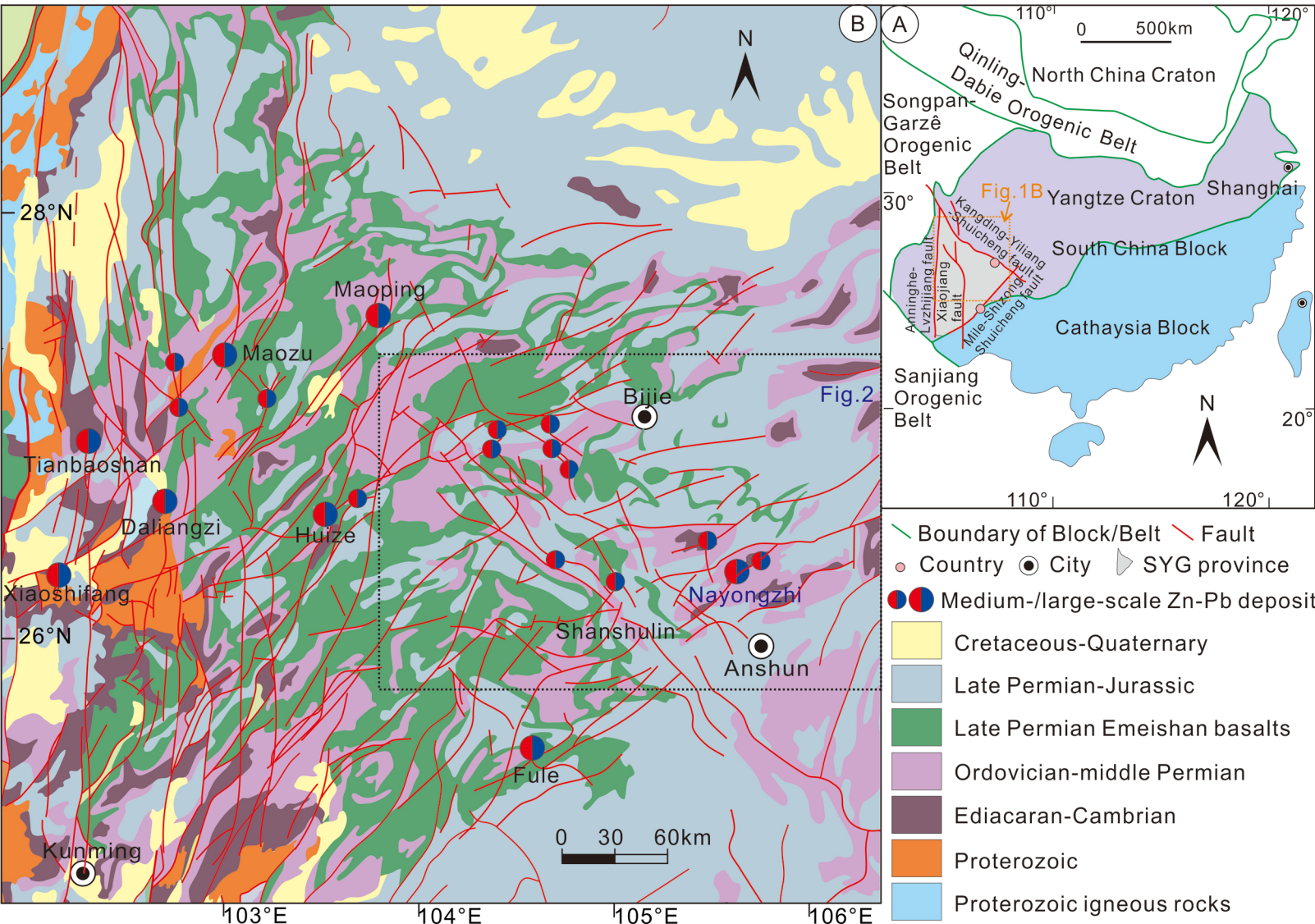


Fig. 2

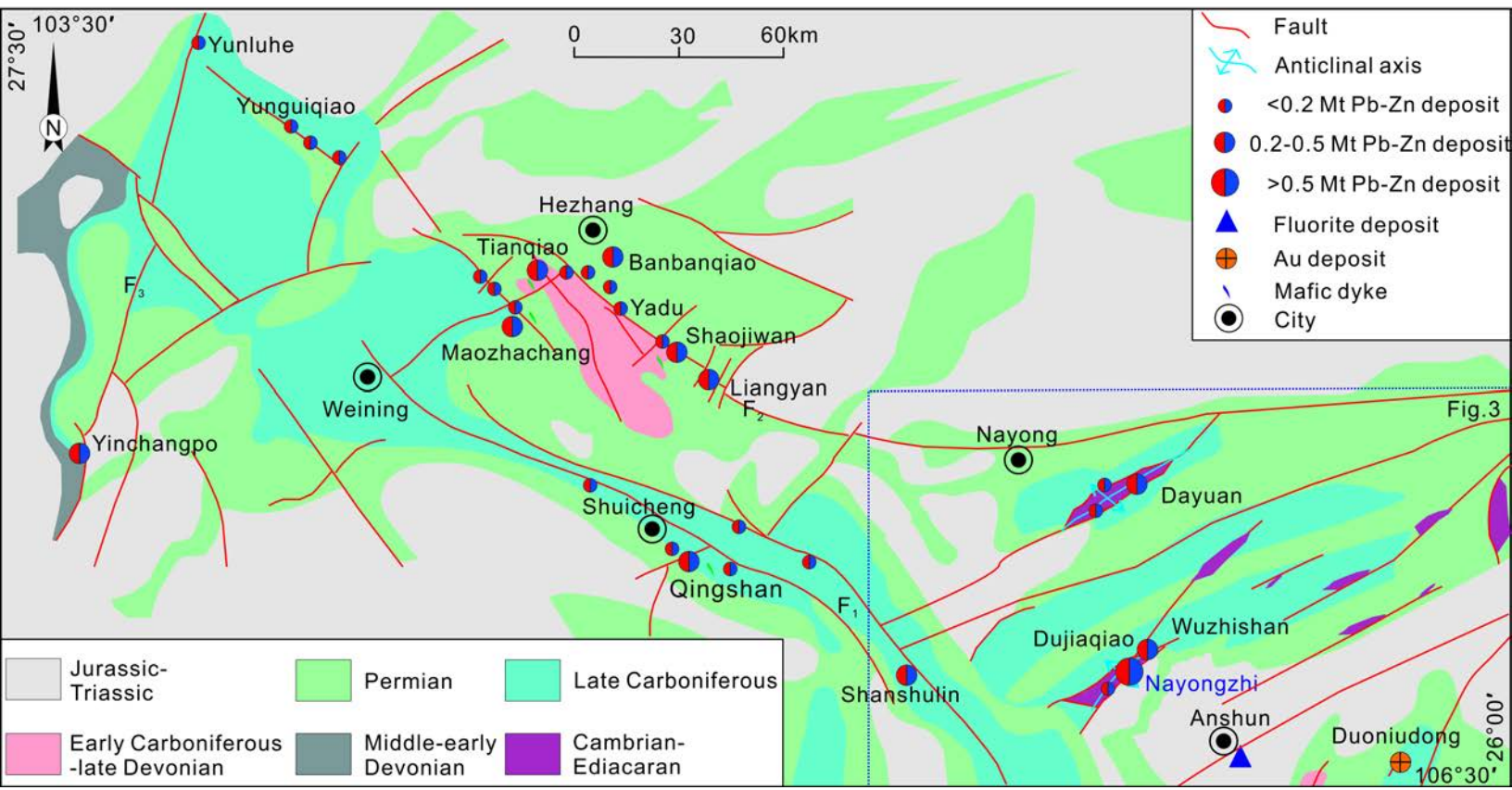


Fig.3

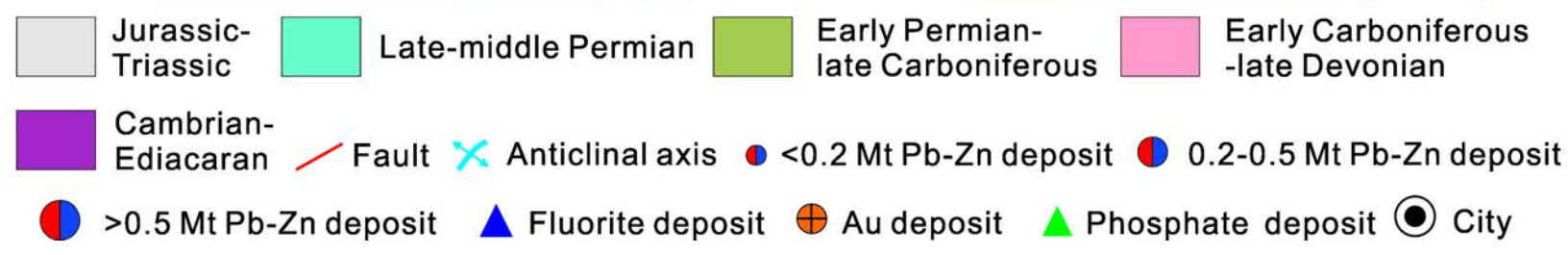
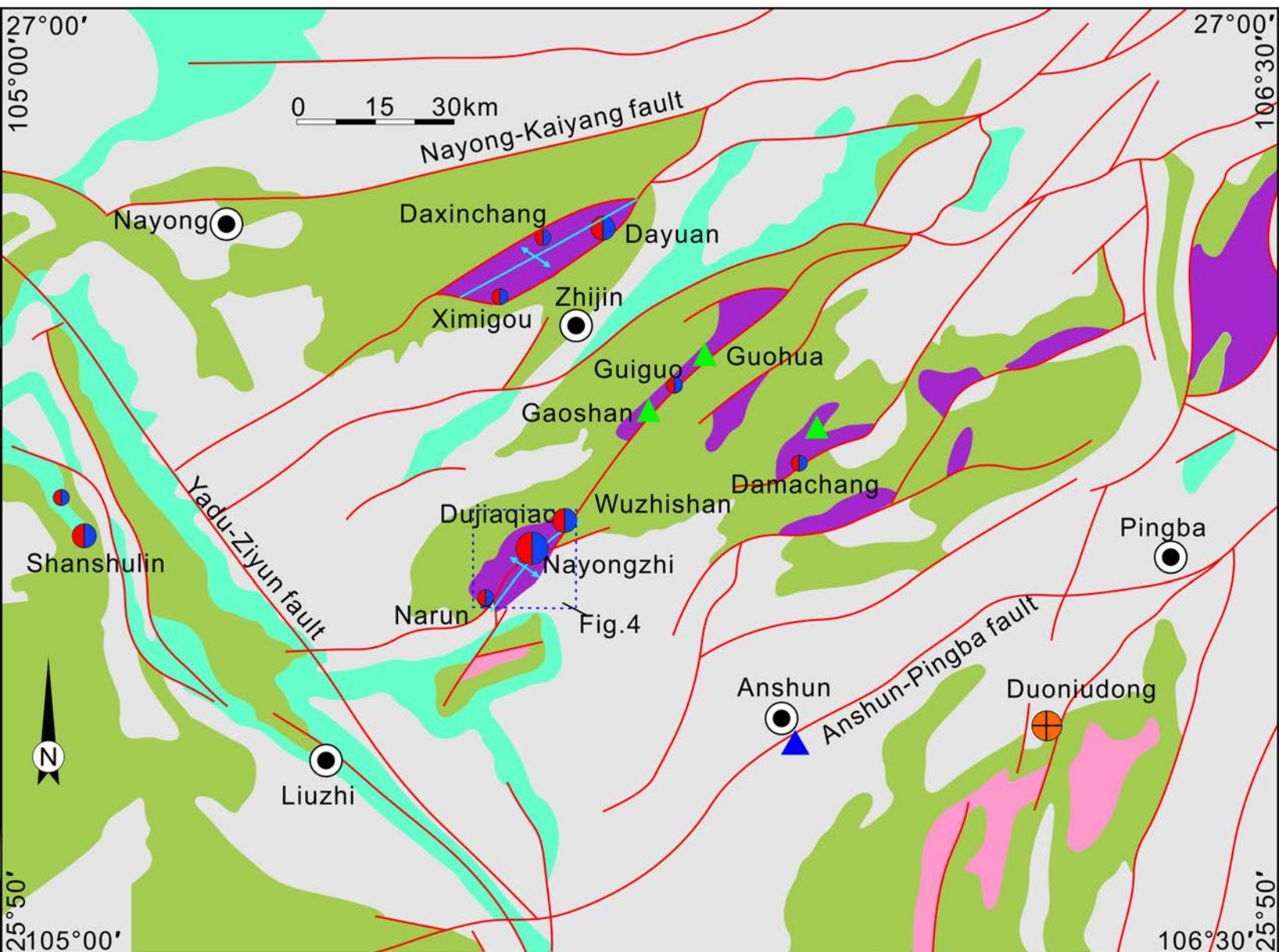
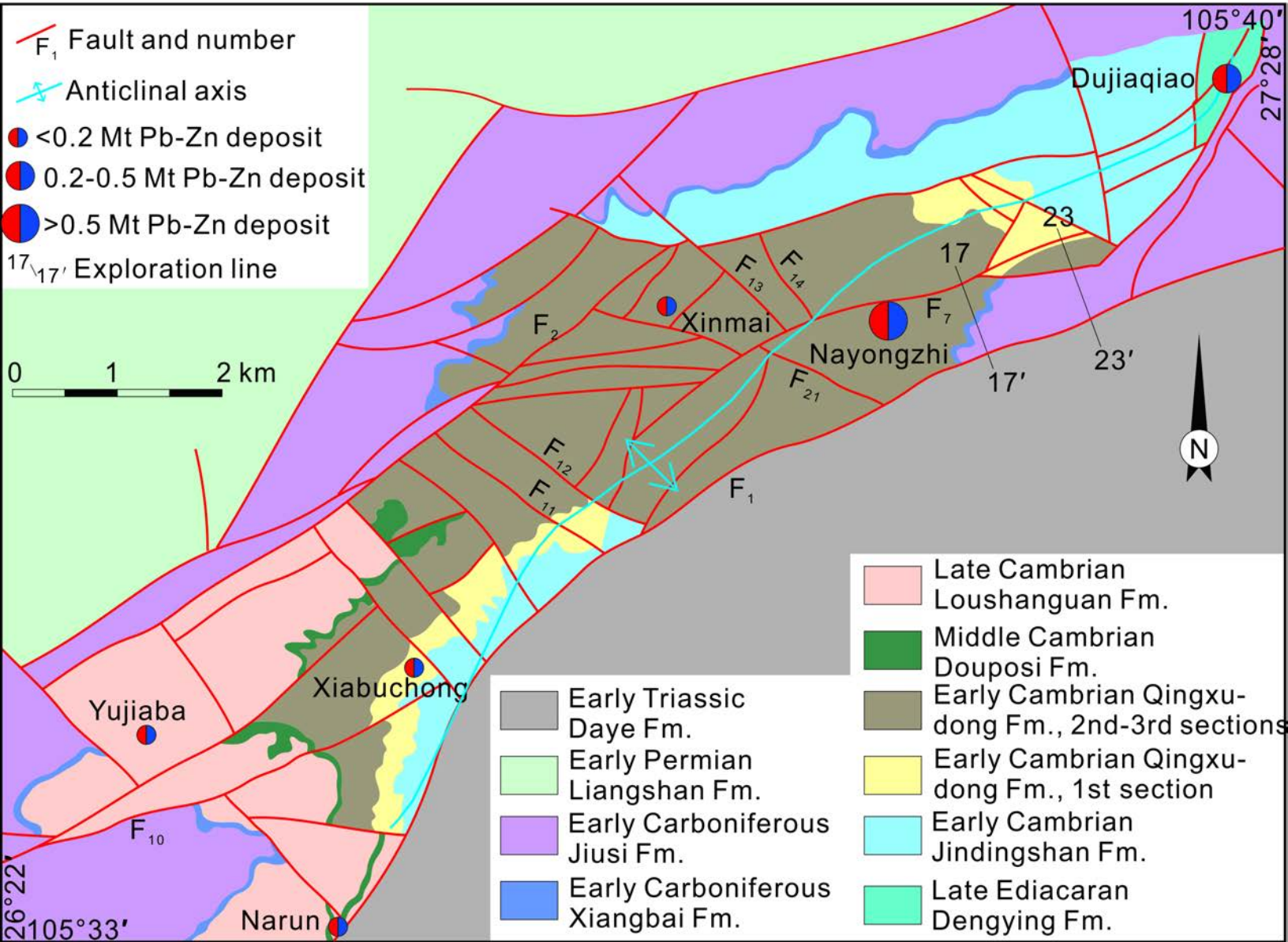




Fig. 4



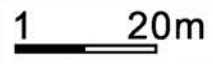
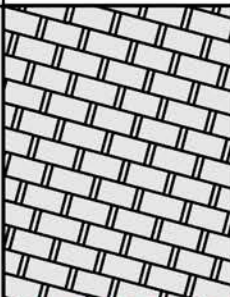


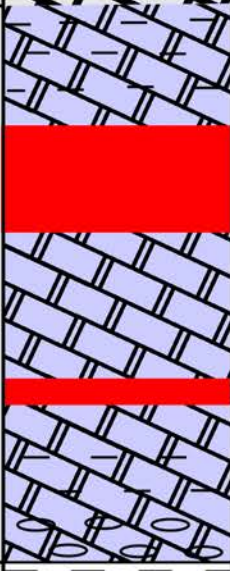
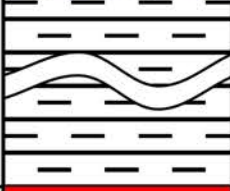
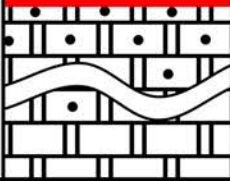
Strata		m	Petrology
Early Cambrian Qingxudong Fm., 3rd section		40-80	Gray fine-layer fine-grained argillaceous limestone and dolostone with rare light gray fine-grained limestone and dolostone.
			Gray thick-layer fine- to medium-grained limestone and dolostone with rare oolite and tumor dolostone.
Early Cambrian Qingxudong Fm., 2nd section 2nd layer		70-90	Gray medium- to thick-layer powder- to medium-crystal dolostone with rare argillaceous limestone and dolostone. Group III ore bodies.
Early Cambrian Qingxudong Fm., 2nd section 1st layer		60-80	(6th) dark gray medium- to thick-layer fine-grained limestone and dolostone with irregular carbon argillaceous stripes, 20-40 m thick; (5th) gray thick-layer medium- to coarse-grained silty limestone and dolostone, 20 m thick;
			(4th) gray thick-layer coarse-grained limestone and dolostone with geode, 0-10 m thick; (3rd) gray thick-layer oolite and tumor dolostone, 20-30 m thick;
Early Cambrian Qingxudong Fm., 1st section		105-160	(2nd) dark gray thick-layer argillaceous limestone and dolostone, 30-50 m thick; (1st) gray middle- to thick-layer oolite and tumor dolostone, 5-10 m thick. Group I and II ore bodies.
Early Cambrian Jindingshan Fm.		> 100	Dark gray, greyish-green fine- to medium-grained argillaceous siltstone and shale.
Late Ediacaran Dengying Fm.		> 100	Gray medium- to thick-layer dolarenite, algae-bearing dolostone and powder crystal limestone and dolostone.

Fig. 6

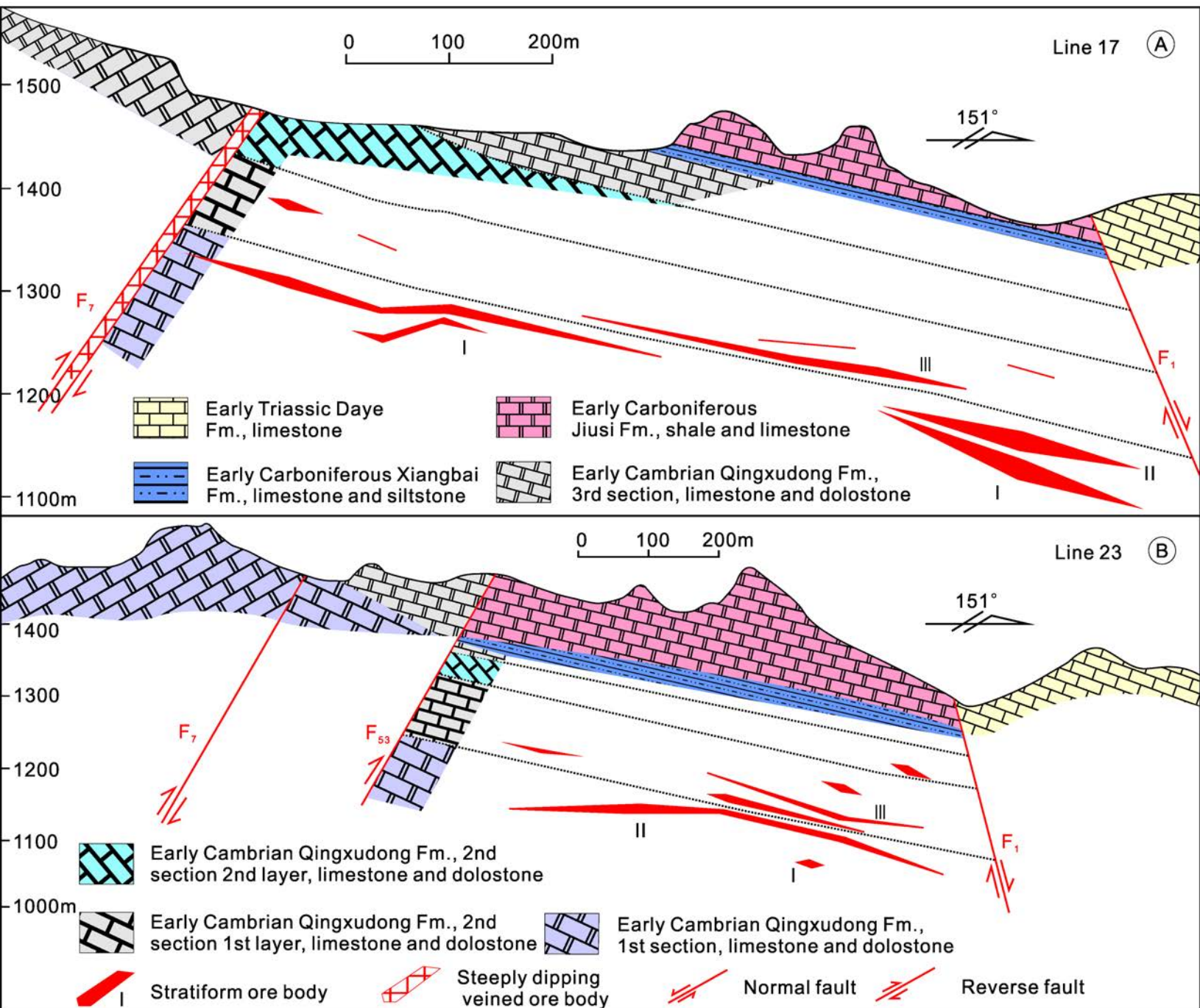


Fig. 7

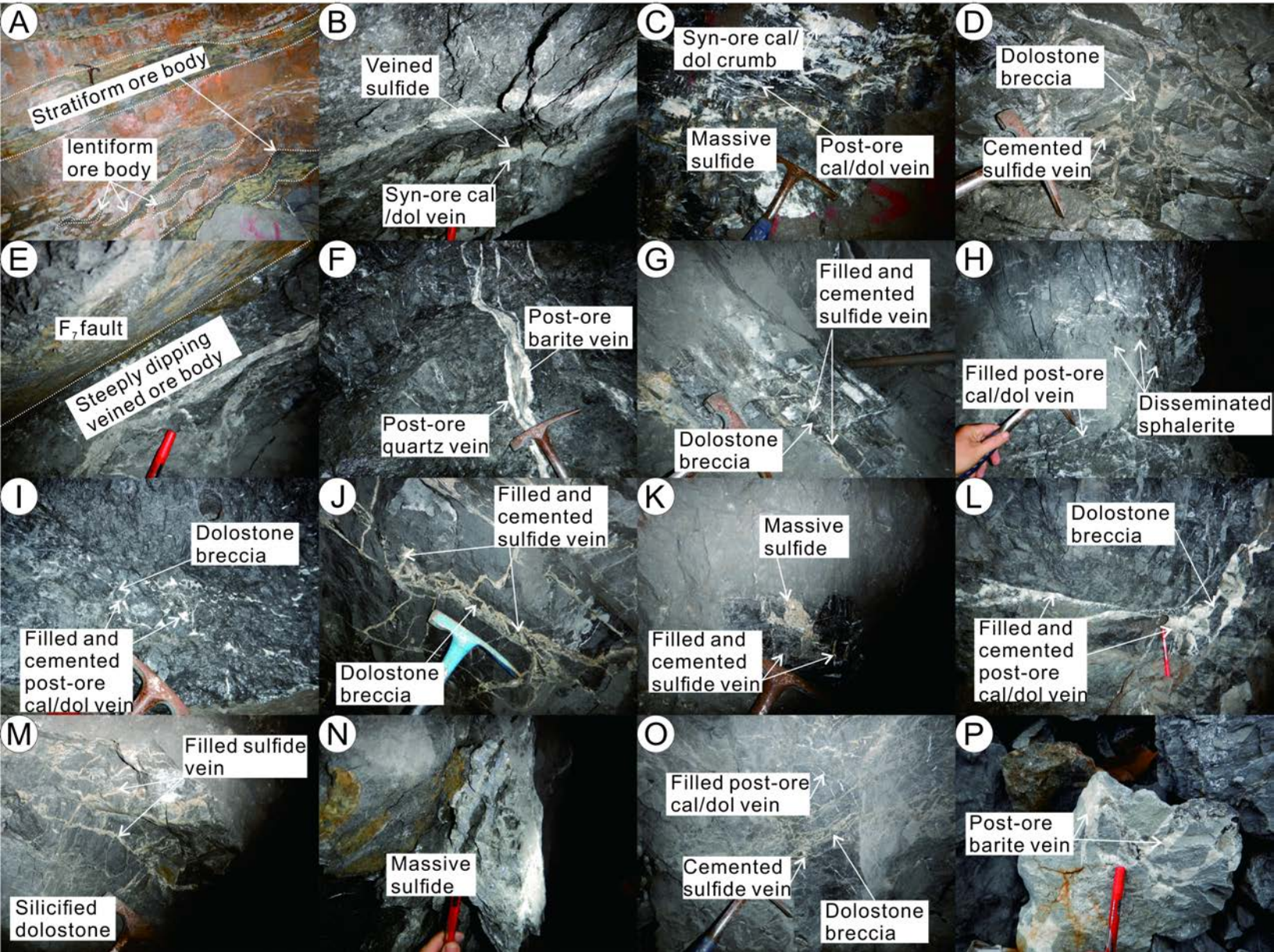


Fig. 8

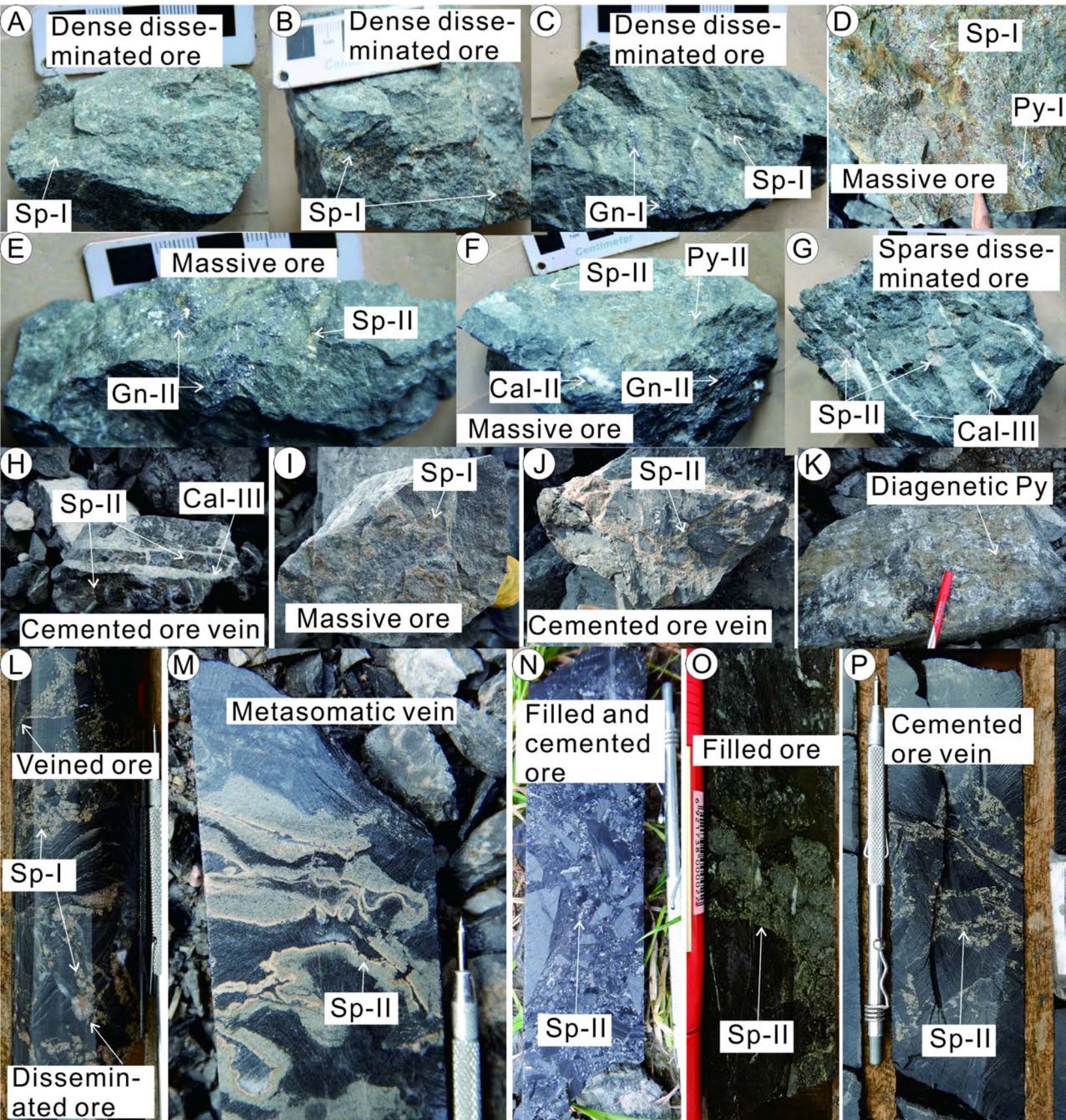


Fig.9

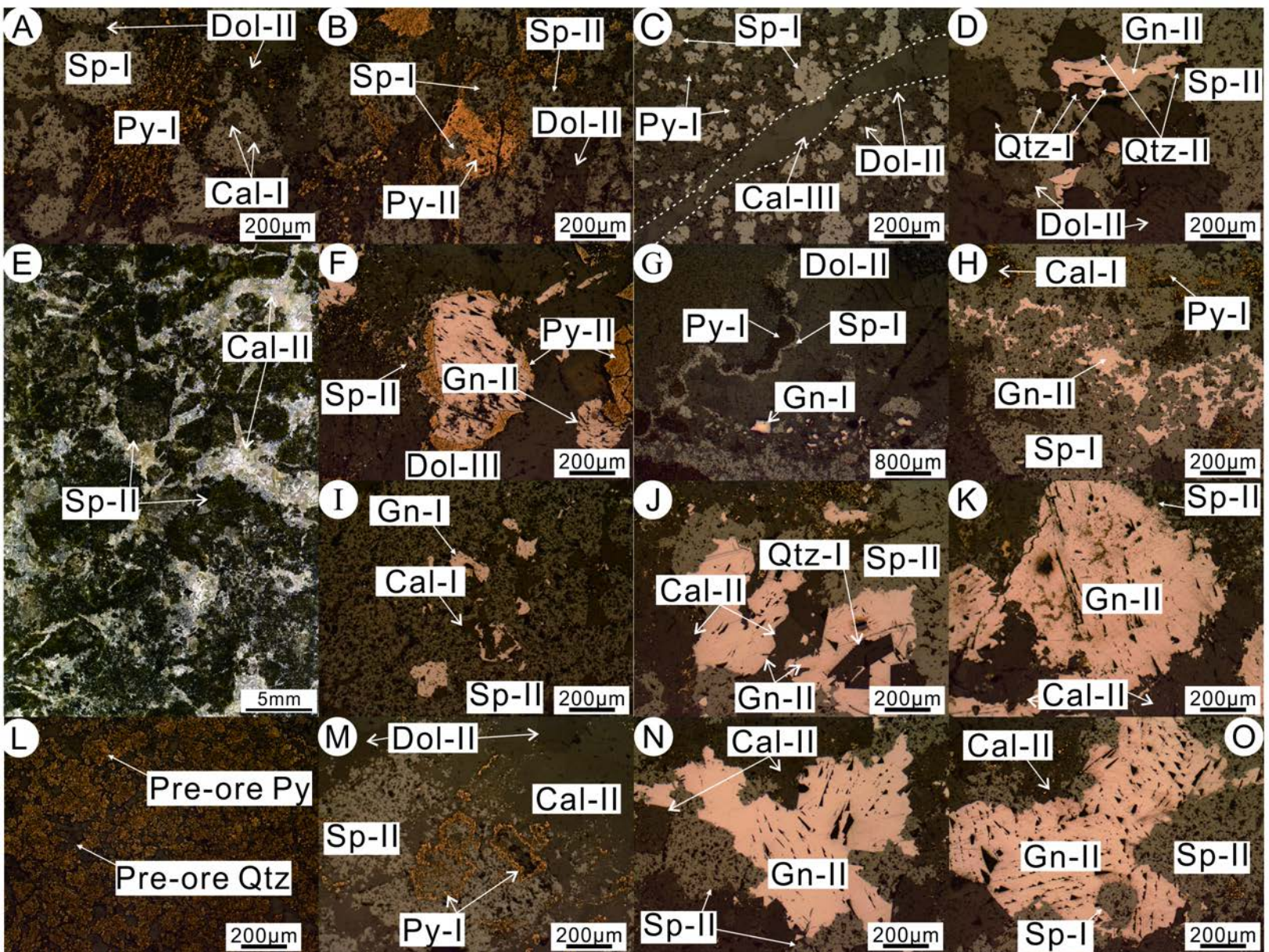


Fig. 10

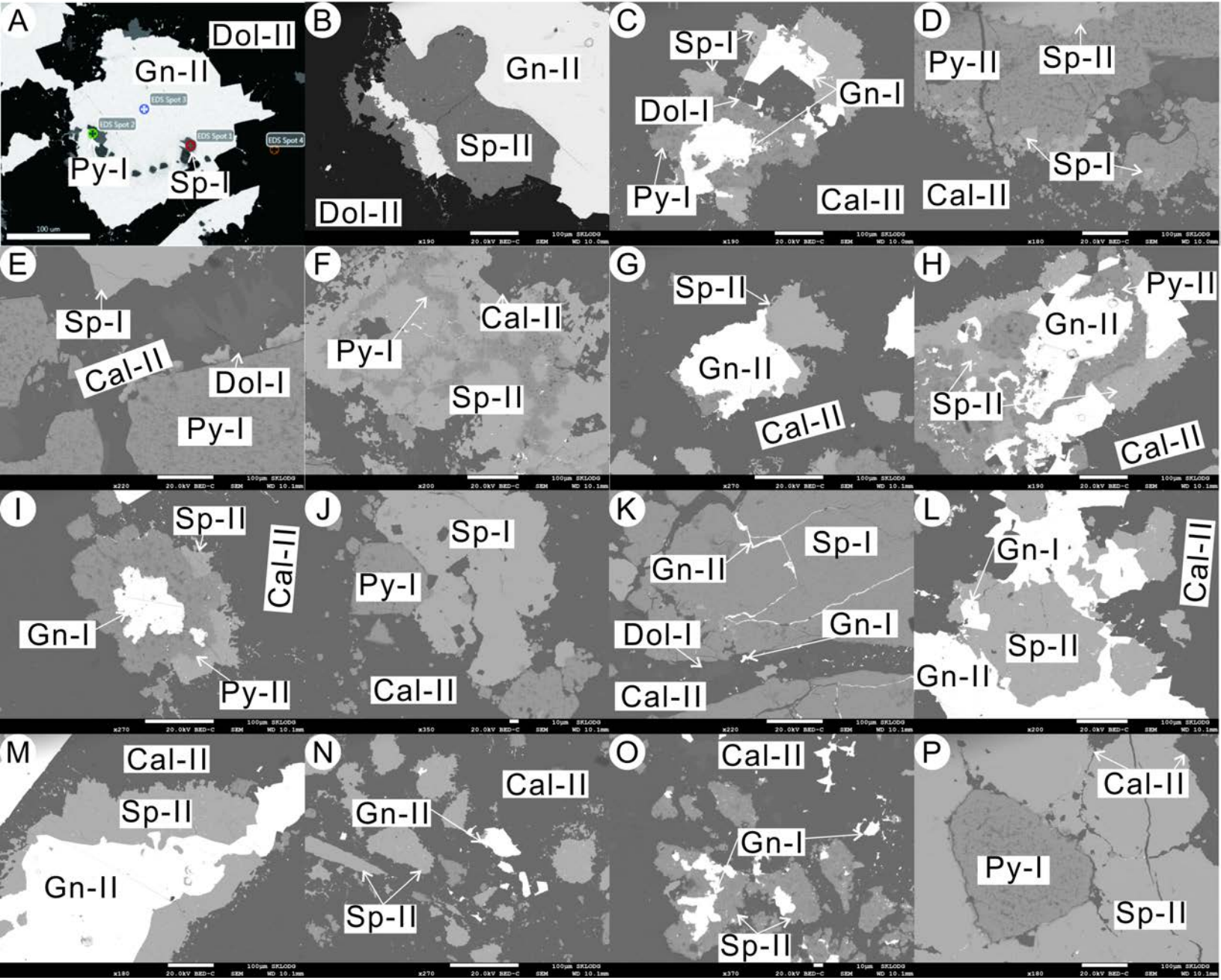


Fig.11

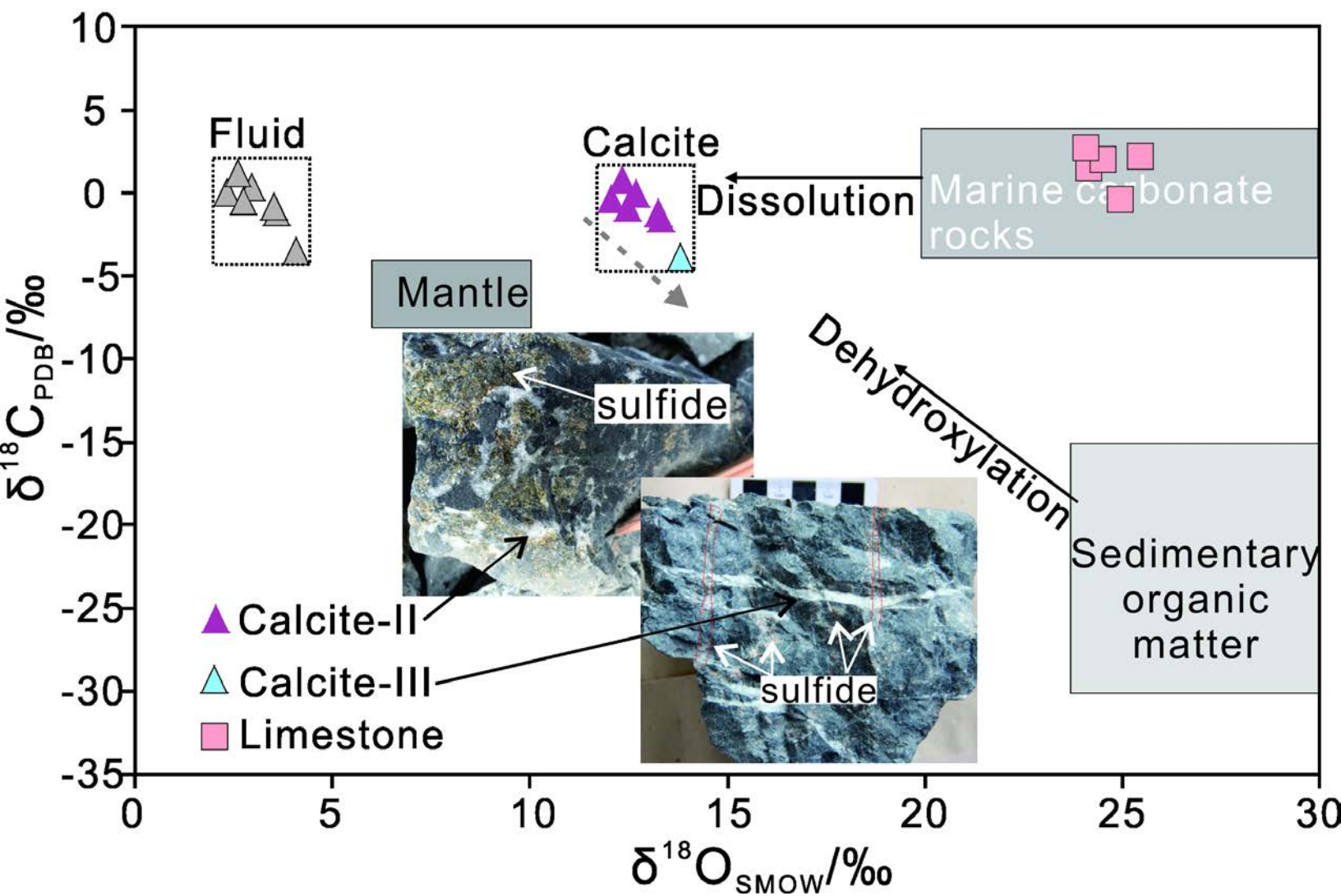
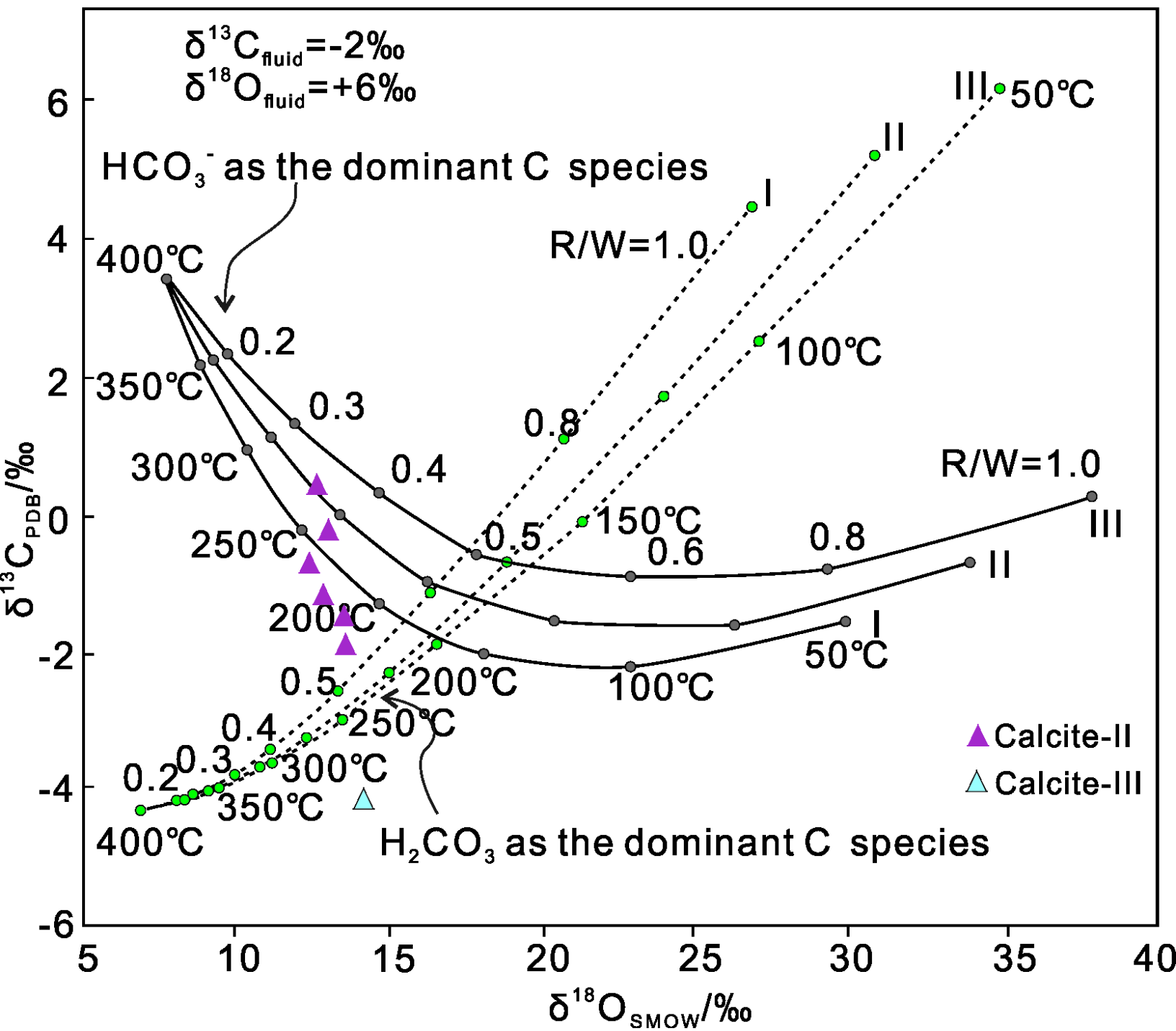




Fig. 12



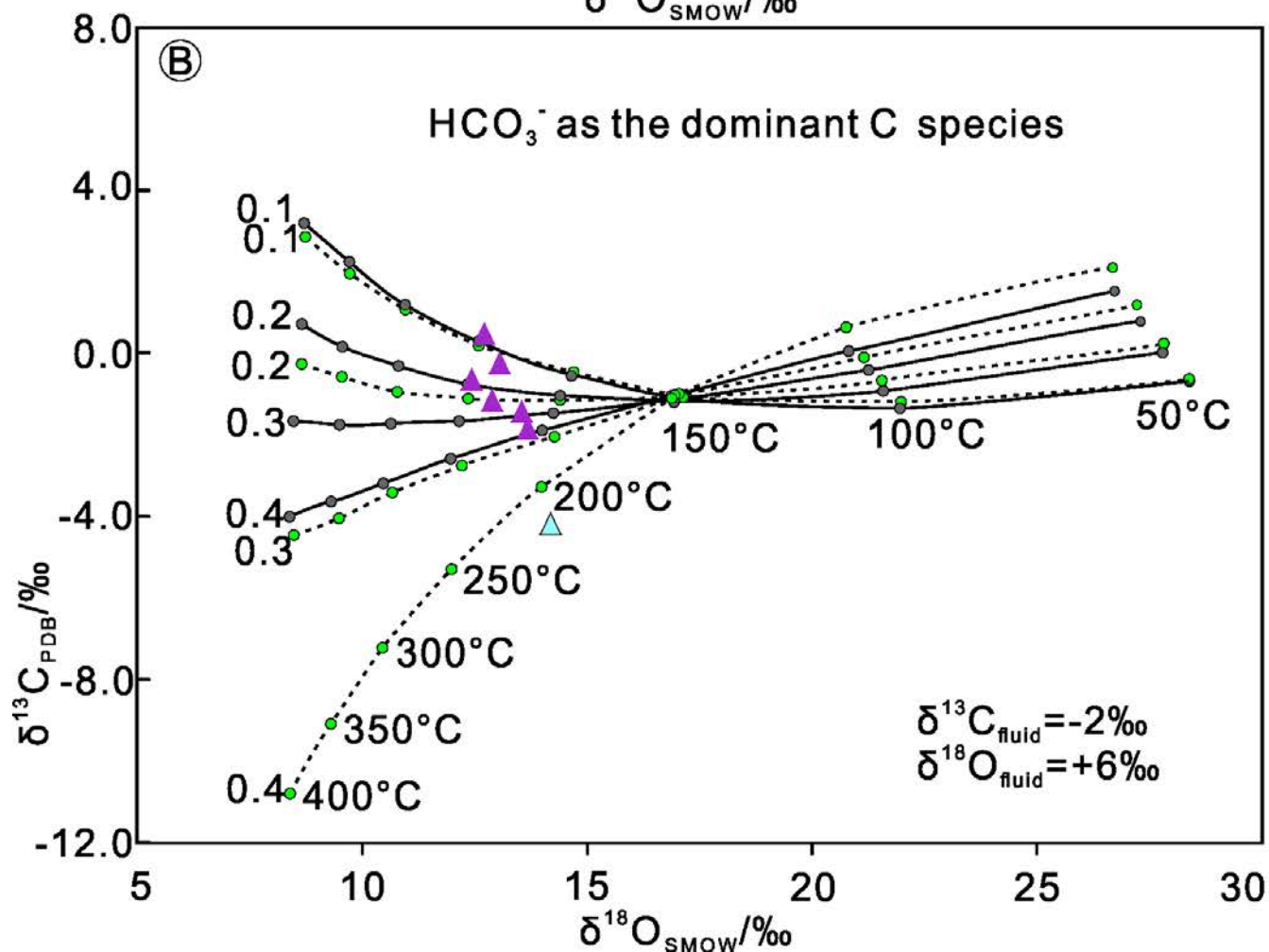
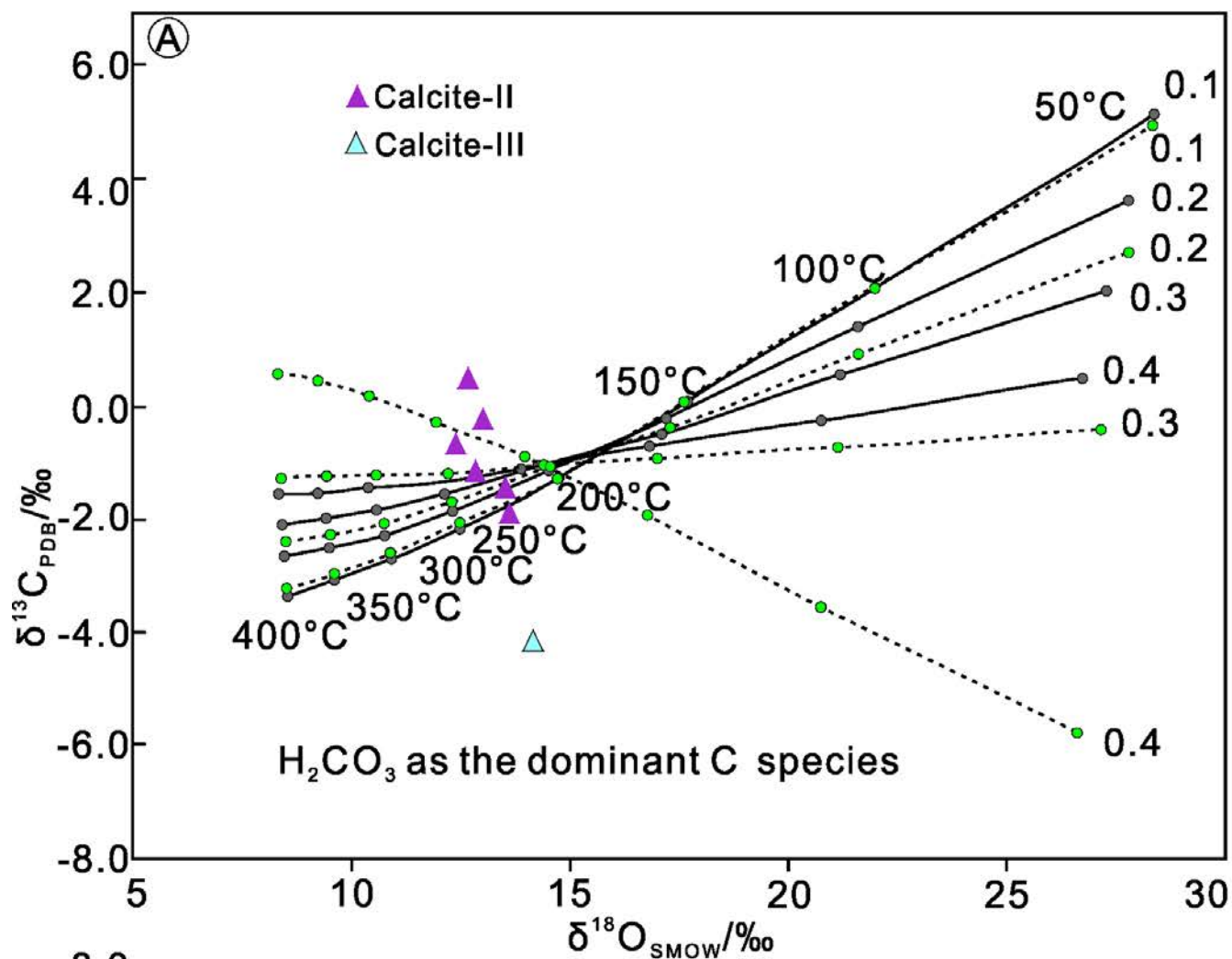


Fig. 14

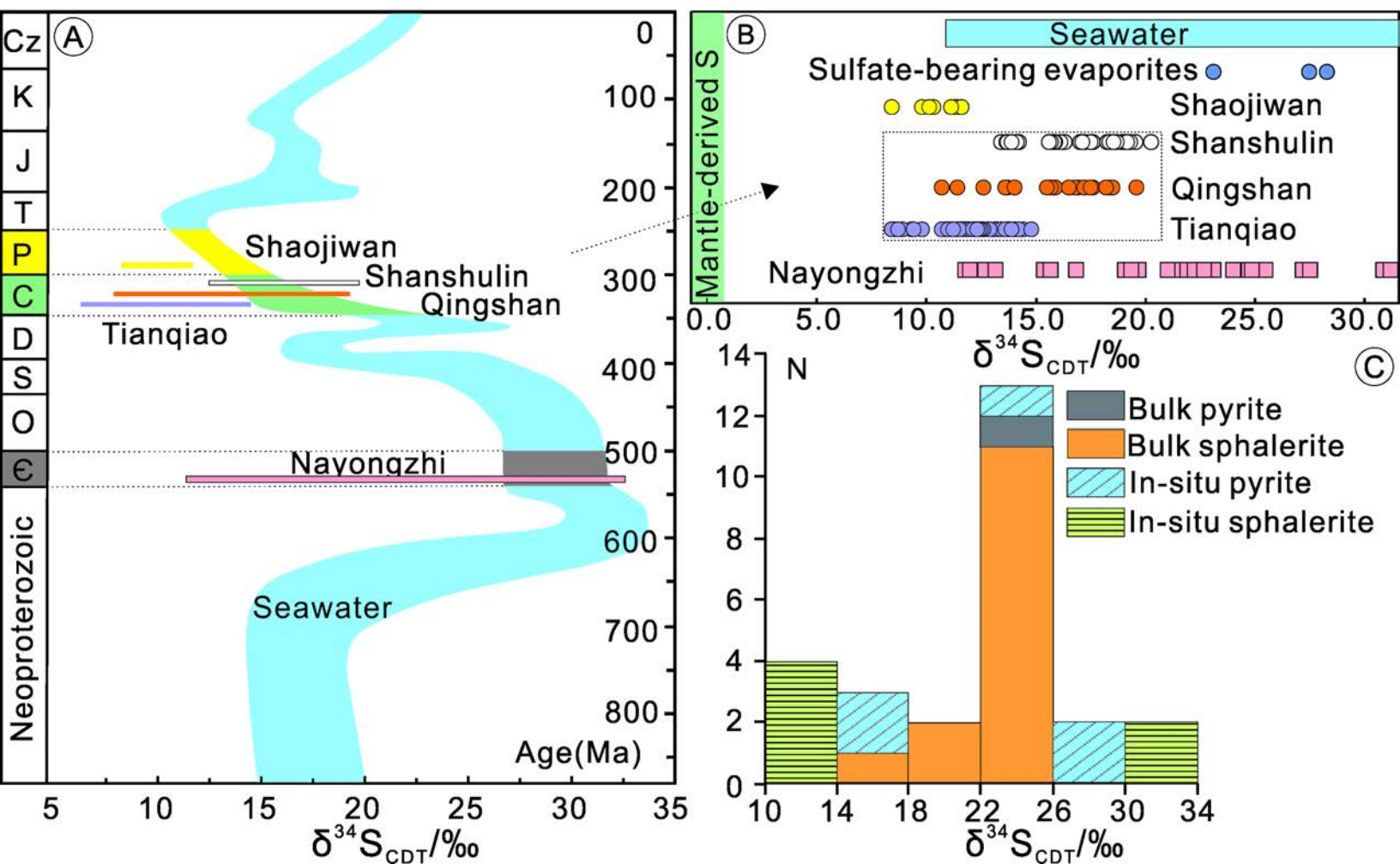
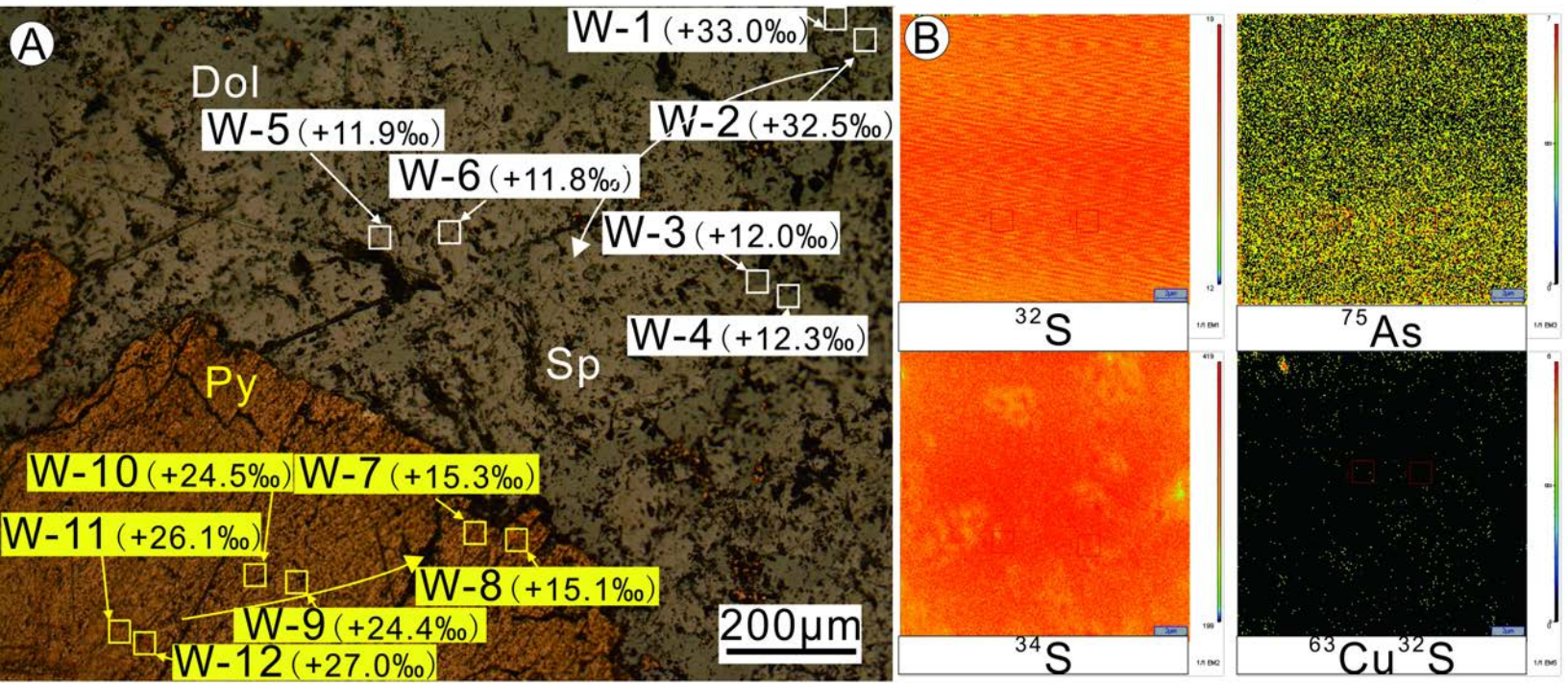


Fig. 15



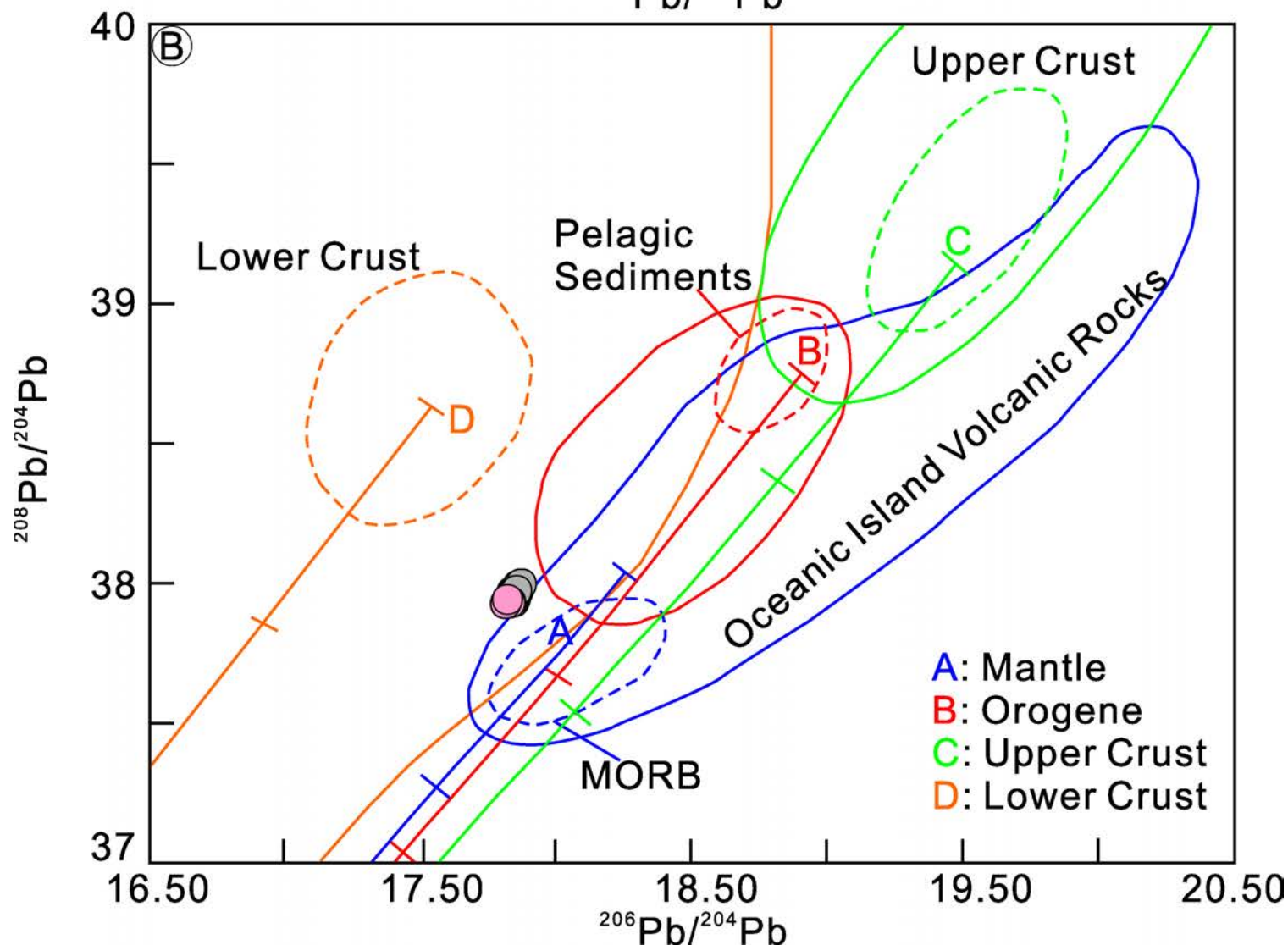
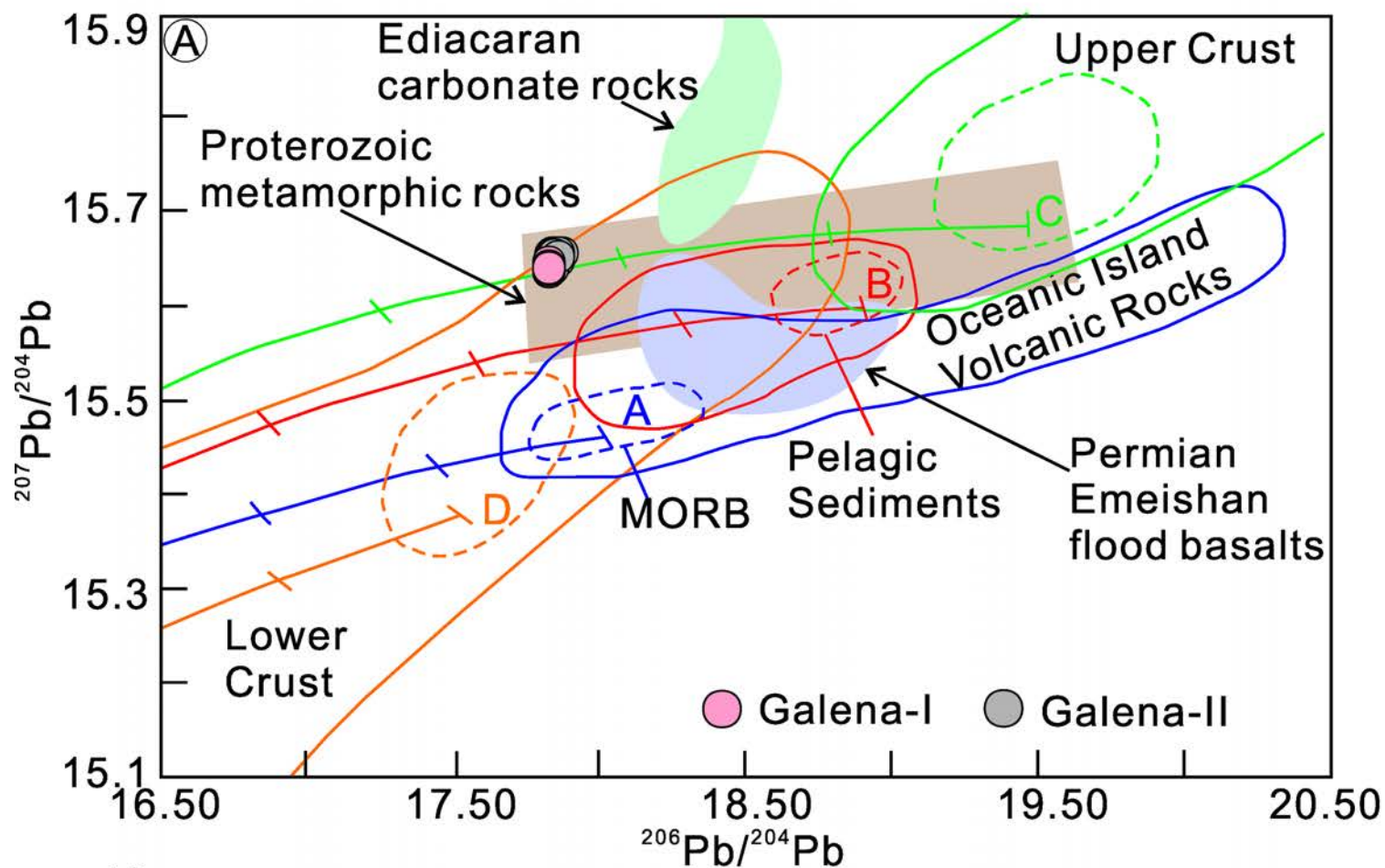


Fig. 17

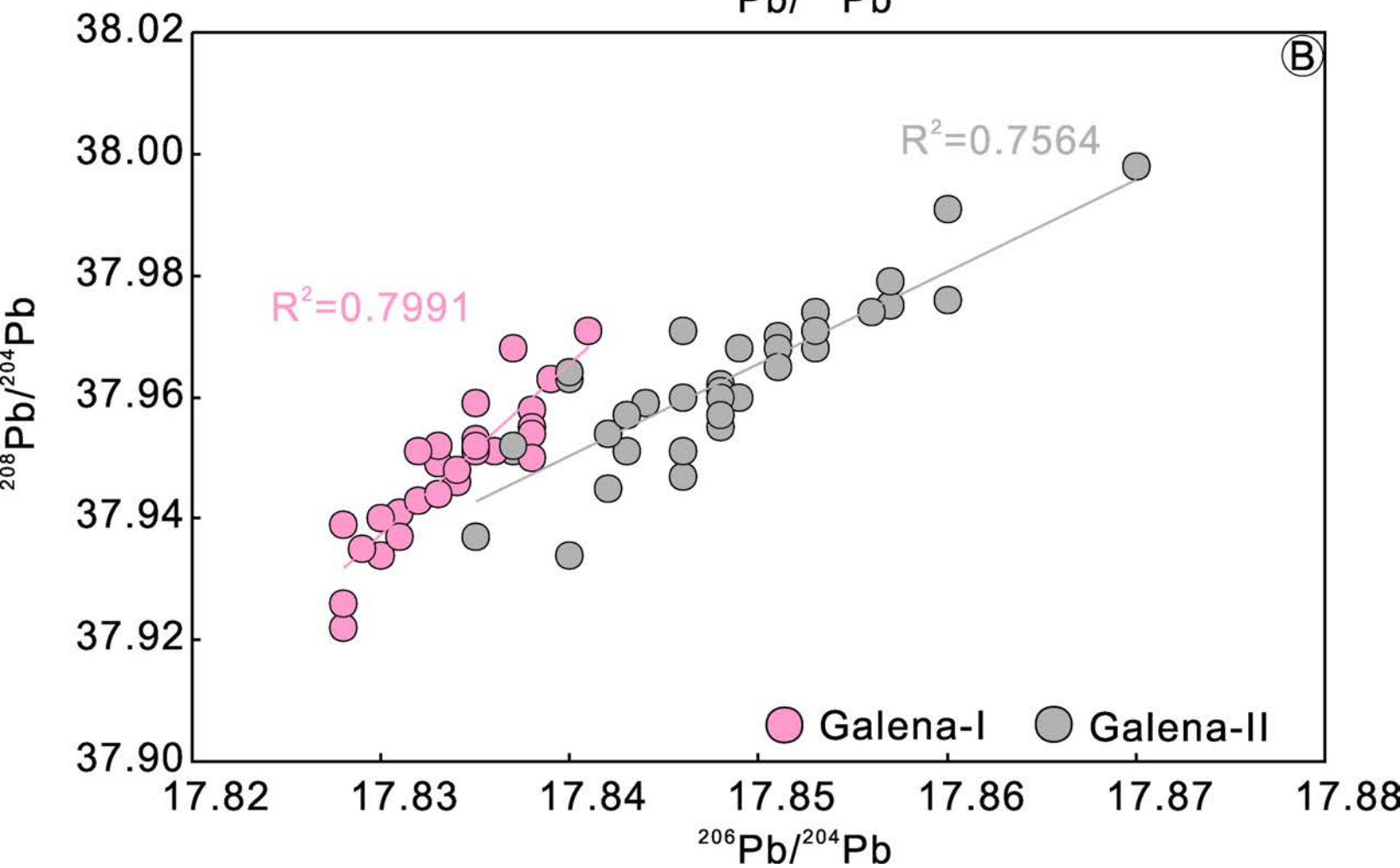
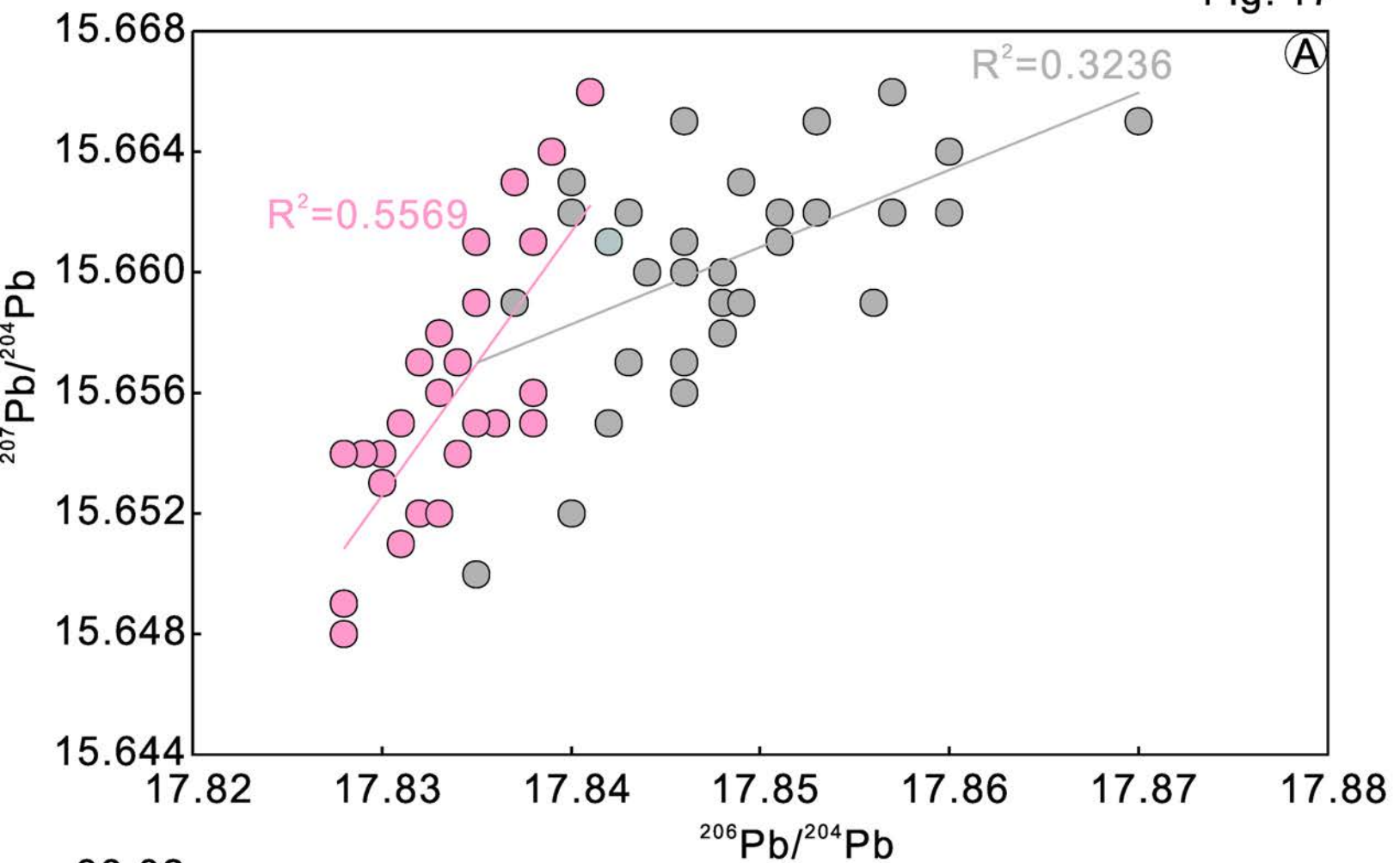


Fig. 18

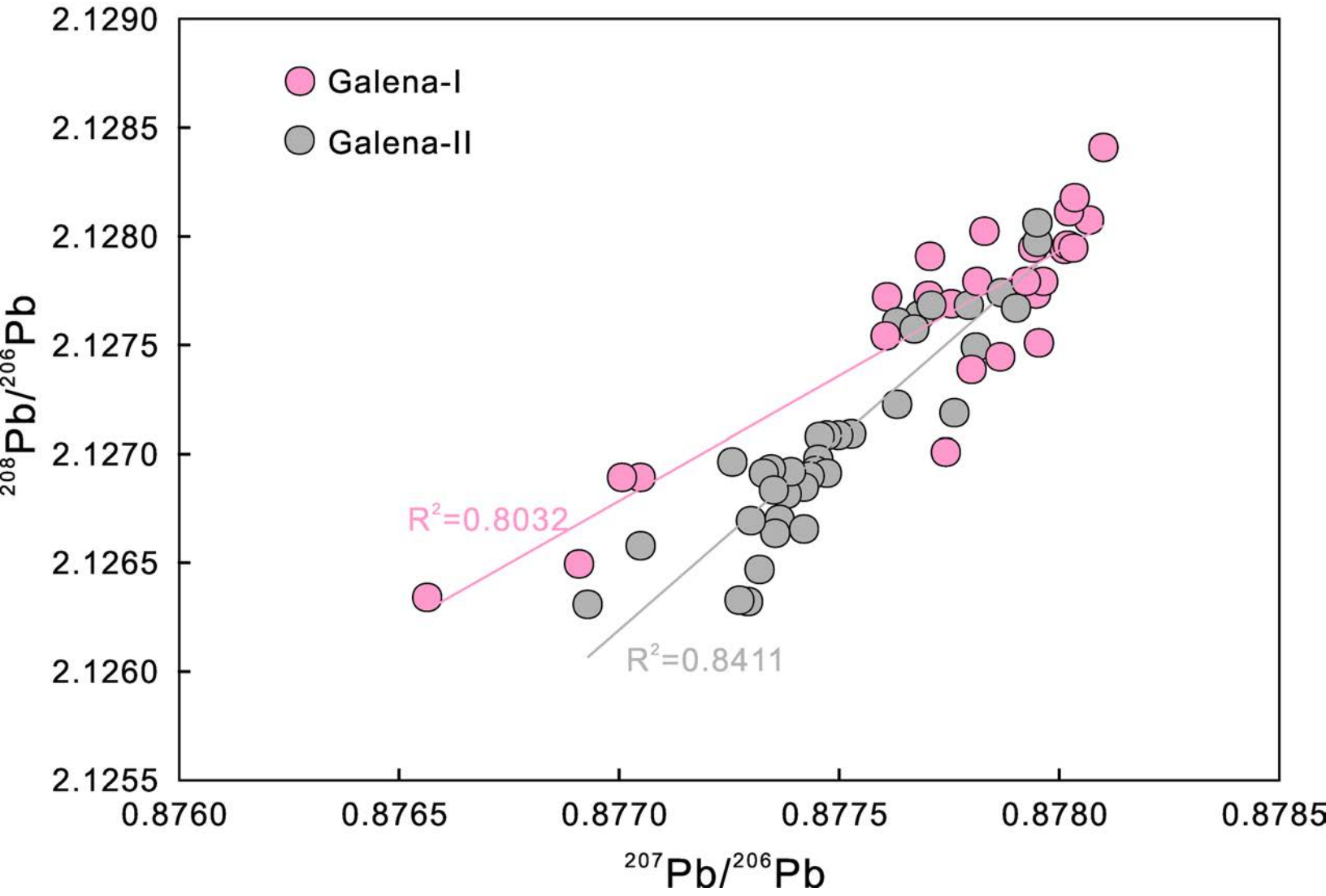
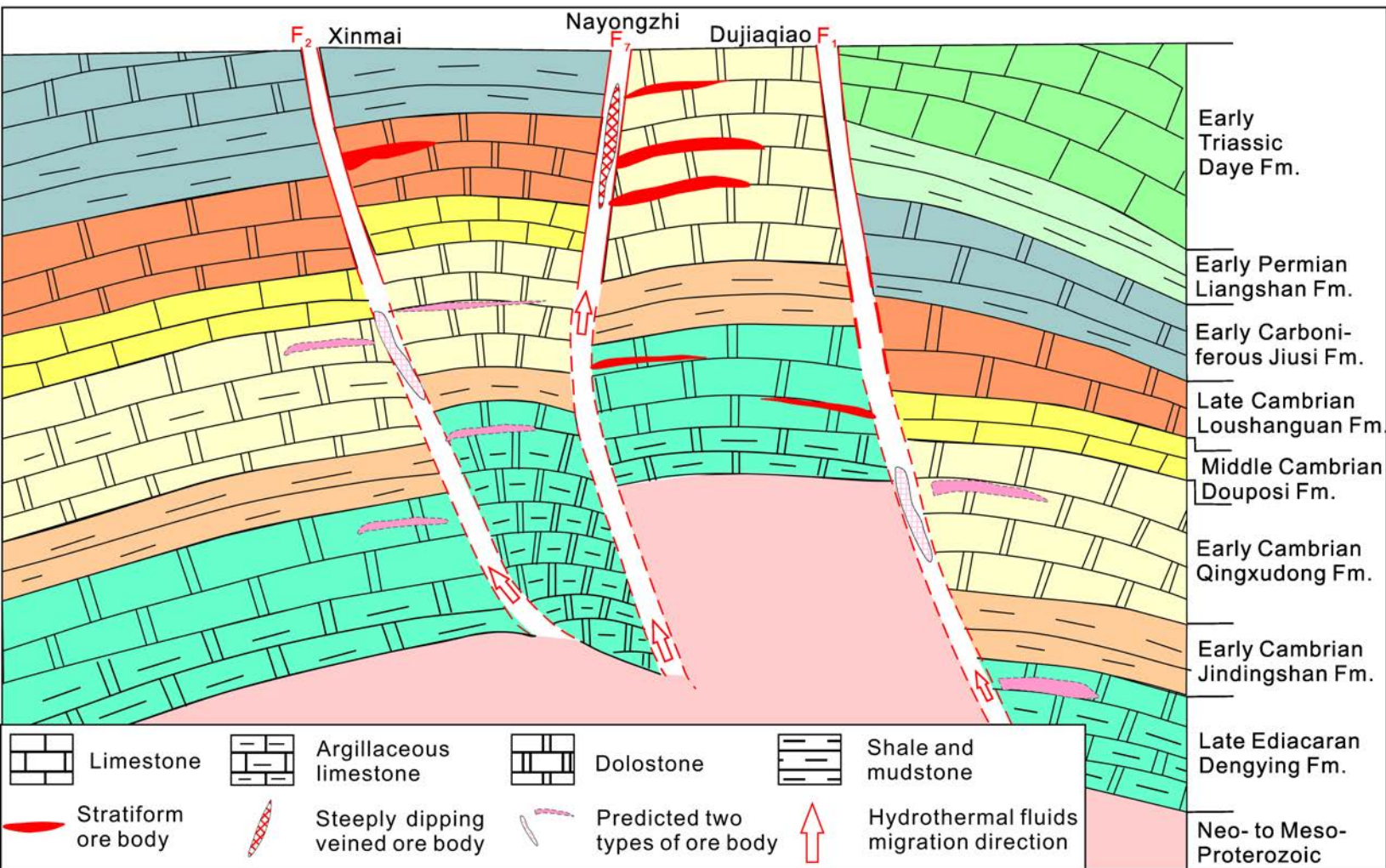
















Fig. 19





**Table 1 Mineral paragenesis in the Nayongzhi Zn-Pb deposit**

Period	Diagenetic	Hydrothermal		Oxidized	
Stage		Sulfide-(quartz-carbonates)		Quartz-carbonates-barite	
Mineral assemblage	Pyrite + quartz + dolomite	<b>Sphalerite</b> + pyrite + galena + quartz + calcite/dolomite	<b>Sphalerite + galena</b> + pyrite + quartz + calcite/dolomite	Quartz + calcite/dolomite + barite	Oxidized Leached
Phase		I	II	III	
Pyrite					
Sphalerite					
Galena					
Quartz					
Calcite					
Dolomite					
Barite					
Limonite					
Cerussite					
Smithsonite					
Hemimorphite					

**Table 2 C-O isotopic compositions of calcite and limestone in the Nayongzhi deposit**

No.	Mineral/Rock	$\delta^{13}\text{C}_{\text{PDB}}/\text{‰}$	$\delta^{18}\text{O}_{\text{PDB}}/\text{‰}$	$\delta^{18}\text{O}_{\text{SMOW}}/\text{‰}$	$\delta^{13}\text{C}_{\text{CO}_2}/\text{‰}^1$	$\delta^{18}\text{O}_{\text{H}_2\text{O}}/\text{‰}^2$
H06-6	Calcite-III	-4.1	-16.2	+14.1	-4.2	+4.0
H06-17	Calcite-II	-0.7	-17.9	+12.4	-0.8	+2.3
1290F-4	Calcite-II	-1.9	-16.7	+13.6	-2.0	+3.5
1390Cal	Calcite-II	-0.2	-17.3	+13.0	-0.3	+2.9
1390JP-4	Calcite-II	-1.4	-16.8	+13.6	-1.5	+3.5
1390JP-6	Calcite-II	-1.1	-17.5	+12.9	-1.2	+2.8
1390JP-7	Calcite-II	+0.5	-17.6	+12.7	+0.4	+2.6
YH1220-1	Limestone	+0.2	-6.5	+24.2		
YH1220-2	Limestone	+0.6	-6.2	+24.5		
YH1220-3	Limestone	+0.8	-5.2	+25.5		
YH1220-4	Limestone	+1.3	-6.6	+24.1		
YH1220-5	Limestone	-1.7	-5.7	+25.0		

$\delta^{18}\text{O}_{\text{SMOW}} = 1.03086 \times \delta^{18}\text{O}_{\text{PDB}} + 30.86$  (Friedman and O'Neil 1977); the error is  $\pm 0.2\text{‰}$  ( $2\sigma$ ) for  $\delta^{13}\text{C}$  and  $\pm 1\text{‰}$  ( $2\sigma$ ) for  $\delta^{18}\text{O}$ ;

<sup>1</sup>  $1000\ln\alpha_{(\text{CO}_2 - \text{Calcite})} = -2.4612 + 7.663 \times 10^3 / (t + 273.15) - 2.988 \times 10^6 / (t + 273.15)^2$  (Bottinga, 1968);

<sup>2</sup>  $1000\ln\alpha_{(\text{Calcite} - \text{H}_2\text{O})} = 2.78 \times 10^6 / (t + 273.15)^2 - 3.39$  (O'Neil et al., 1969);

t = 180°C, based on temperature analysis of fluid inclusion in quartz-II (Zhu et al., 2016b).

**Table 3 Bulk S and in situ S isotopic compositions of sulfide minerals in the Nayongzhi deposit**

No.	Obj.	Stage	$\delta^{34}\text{S}_{\text{CDT}}/\text{‰}$	Note
2015HT-2-0	Pyrite	Stage I	+22.06	
2015JP-1-1	Pyrite	Stage I	+18.12	
2015HT-2-1	Yellow sphalerite	Stage II	+21.04	
2015HT-2-2	Brown-yellow sphalerite	Stage II	+22.42	
2015HT-2-3	Brown sphalerite	Stage I	+22.51	
2015HT-1-1	Yellow sphalerite	Stage II	+24.59	
2015HT-1-2	Brown-yellow sphalerite	Stage II	+23.60	
2015HT-1-3	Brown-red sphalerite	Stage I	+24.73	Whole-mineral
2015HT-1-3	Brown-red sphalerite	Stage I	+24.79	
2015HT-5-1	Yellow sphalerite	Stage II	+23.57	
2015HT-5-2	Brown-yellow sphalerite	Stage II	+23.64	
2015HT-5-3	Brown-red sphalerite	Stage I	+23.27	
2015HT-4-1	Yellow sphalerite	Stage II	+17.17	
2015HT-4-2	Brown-yellow sphalerite	Stage II	+21.95	
2015HT-4-3	Brown sphalerite	Stage I	+24.17	
2015HT-4-3	Brown sphalerite	Stage I	+24.20	
W-1	Sphalerite-I	Core	+33.0	
W-2	Sphalerite-I	Core	+32.5	
W-3	Sphalerite-I	Rim	+12.0	
W-4	Sphalerite-I	Rim	+12.3	
W-5	Sphalerite-I	Rim	+11.9	
W-6	Sphalerite-I	Rim	+11.8	In situ
W-7	Pyrite-I	Rim	+15.1	
W-8	Pyrite-I	Rim	+15.3	
W-9	Pyrite-I	Rim	+24.4	
W-10	Pyrite-I	Rim	+24.5	
W-11	Pyrite-I	Core	+26.1	
W-12	Pyrite-I	Core	+27.0	

The error is  $\pm 0.2\text{‰}$  ( $2\sigma$ ) for bulk  $\delta^{34}\text{S}$  and  $\pm 0.2\text{‰}$  (1s) for in situ  $\delta^{34}\text{S}$ .

**Table 4 In situ Pb isotopic compositions of galena in the Nayongzhi deposit**

Spot	Stage	$^{206}\text{Pb}/^{204}\text{Pb}$	1s	$^{207}\text{Pb}/^{204}\text{Pb}$	1s	$^{208}\text{Pb}/^{204}\text{Pb}$	1s	$\mu$	$^{208}\text{Pb}/^{206}\text{Pb}$	1s	$^{207}\text{Pb}/^{206}\text{Pb}$	1s
K-2-01	Galena-I	17.830	0.002	15.654	0.003	37.934	0.007	9.65	2.1274	0.0001	0.87786	0.00003
K-2-02	Galena-I	17.833	0.003	15.656	0.003	37.949	0.008	9.65	2.1278	0.0001	0.87792	0.00004
K-2-03	Galena-I	17.829	0.002	15.654	0.003	37.935	0.007	9.65	2.1275	0.0001	0.87795	0.00003
K-2-04	Galena-I	17.828	0.002	15.648	0.003	37.922	0.007	9.64	2.1270	0.0001	0.87774	0.00003
K-2-05	Galena-I	17.831	0.003	15.655	0.003	37.941	0.009	9.65	2.1277	0.0002	0.87794	0.00004
K-2-06	Galena-I	17.828	0.002	15.649	0.002	37.926	0.007	9.64	2.1274	0.0001	0.87780	0.00003
K-2-07	Galena-I	17.834	0.003	15.657	0.003	37.946	0.008	9.65	2.1278	0.0001	0.87793	0.00004
K-2-08	Galena-I	17.838	0.003	15.661	0.003	37.958	0.009	9.66	2.1279	0.0001	0.87793	0.00004
K-2-09	Galena-I	17.837	0.003	15.663	0.003	37.968	0.009	9.67	2.1284	0.0001	0.87809	0.00004
K-2-10	Galena-I	17.828	0.003	15.654	0.003	37.939	0.008	9.65	2.1279	0.0001	0.87803	0.00004
K-2-11	Galena-I	17.835	0.003	15.661	0.003	37.959	0.008	9.66	2.1282	0.0001	0.87803	0.00004
K-2-12	Galena-I	17.839	0.003	15.664	0.003	37.963	0.008	9.67	2.1279	0.0001	0.87801	0.00004
K-2-13	Galena-I	17.833	0.003	15.658	0.003	37.952	0.009	9.66	2.1281	0.0002	0.87802	0.00004
K-2-14	Galena-I	17.835	0.003	15.659	0.003	37.953	0.008	9.66	2.1278	0.0001	0.87796	0.00003
K-2-15	Galena-I	17.841	0.003	15.666	0.003	37.971	0.009	9.67	2.1281	0.0002	0.87806	0.00004
K-2-16	Galena-I	17.832	0.003	15.657	0.004	37.951	0.01	9.65	2.1279	0.0001	0.87801	0.00004
HA1-5-06	Galena-I	17.838	0.002	15.656	0.002	37.955	0.006	9.65	2.1277	0.0001	0.87770	0.00003
HA1-5-07	Galena-I	17.836	0.003	15.655	0.003	37.951	0.008	9.65	2.1279	0.0001	0.87770	0.00003
HA1-5-08	Galena-I	17.832	0.002	15.652	0.003	37.943	0.007	9.64	2.1269	0.0001	0.87700	0.00003
HA1-5-09	Galena-I	17.834	0.002	15.654	0.002	37.948	0.006	9.65	2.1269	0.0001	0.87705	0.00002
HA1-5-10	Galena-I	17.833	0.002	15.652	0.003	37.944	0.007	9.64	2.1265	0.0001	0.87691	0.00002
HA1-5-11	Galena-I	17.835	0.002	15.655	0.002	37.951	0.007	9.65	2.1263	0.0001	0.87656	0.00002
HA1-5-12	Galena-I	17.838	0.002	15.655	0.002	37.954	0.006	9.65	2.1277	0.0001	0.87761	0.00002
HA1-5-13	Galena-I	17.838	0.003	15.655	0.003	37.950	0.008	9.65	2.1275	0.0001	0.87760	0.00003
HA1-5-14	Galena-I	17.835	0.002	15.655	0.003	37.952	0.007	9.65	2.1280	0.0001	0.87783	0.00003
HA1-5-15	Galena-I	17.830	0.002	15.653	0.003	37.940	0.007	9.65	2.1278	0.0001	0.87781	0.00003
HA1-5-16	Galena-I	17.831	0.002	15.651	0.002	37.937	0.006	9.64	2.1277	0.0001	0.87775	0.00002
H2A5-4-01	Galena-II	17.837	0.002	15.659	0.003	37.952	0.007	9.66	2.1277	0.0001	0.87786	0.00003
H2A5-4-02	Galena-II	17.840	0.003	15.663	0.003	37.963	0.009	9.66	2.1280	0.0001	0.87795	0.00004
H2A5-4-03	Galena-II	17.840	0.002	15.662	0.003	37.964	0.007	9.66	2.1280	0.0001	0.87795	0.00003
H2A5-4-04	Galena-II	17.846	0.002	15.665	0.002	37.971	0.007	9.67	2.1277	0.0001	0.87779	0.00003
H2A5-4-05	Galena-II	17.846	0.003	15.661	0.003	37.960	0.008	9.66	2.1271	0.0001	0.87747	0.00003
H2A5-4-06	Galena-II	17.842	0.002	15.655	0.003	37.945	0.007	9.65	2.1269	0.0001	0.87747	0.00003
H2A5-4-07	Galena-II	17.842	0.002	15.661	0.002	37.954	0.007	9.66	2.1272	0.0001	0.87776	0.00003
H2A5-4-08	Galena-II	17.843	0.002	15.662	0.002	37.957	0.007	9.66	2.1275	0.0001	0.87781	0.00003
H2A5-4-09	Galena-II	17.848	0.002	15.658	0.002	37.955	0.007	9.65	2.1265	0.0001	0.87732	0.00003
H2A5-4-10	Galena-II	17.846	0.002	15.656	0.002	37.947	0.007	9.65	2.1263	0.0001	0.87729	0.00003
H2A5-4-11	Galena-II	17.849	0.003	15.659	0.003	37.960	0.007	9.66	2.1267	0.0001	0.87736	0.00003
H2A5-4-12	Galena-II	17.848	0.003	15.66	0.003	37.960	0.007	9.66	2.1269	0.0001	0.87744	0.00003
H2A5-4-13	Galena-II	17.848	0.003	15.66	0.003	37.957	0.007	9.66	2.1267	0.0001	0.87742	0.00003
H2A5-4-14	Galena-II	17.846	0.002	15.657	0.003	37.951	0.007	9.65	2.1266	0.0001	0.87735	0.00003
H2A5-4-15	Galena-II	17.853	0.002	15.665	0.003	37.971	0.007	9.67	2.1270	0.0001	0.87745	0.00003

H2A5-4-16	Galena-II	17.851	0.002	15.661	0.003	37.965	0.007	9.66	2.1268	0.0001	0.87738	0.00003
HA1-5-01	Galena-II	17.860	0.002	15.664	0.003	37.991	0.007	9.66	2.1271	0.0001	0.87745	0.00003
HA1-5-02	Galena-II	17.857	0.002	15.662	0.002	37.979	0.006	9.66	2.1276	0.0001	0.87763	0.00003
HA1-5-03	Galena-II	17.856	0.002	15.659	0.002	37.974	0.005	9.65	2.1276	0.0001	0.87768	0.00003
HA1-5-04	Galena-II	17.870	0.002	15.665	0.002	37.998	0.006	9.66	2.1277	0.0001	0.87771	0.00003
HA1-5-05	Galena-II	17.835	0.003	15.65	0.003	37.937	0.008	9.64	2.1276	0.0001	0.87767	0.00003
1390-JP-12-01	Galena-II	17.851	0.002	15.662	0.002	37.970	0.006	9.66	2.1269	0.0001	0.87734	0.00003
1390-JP-12-02	Galena-II	17.848	0.003	15.659	0.003	37.962	0.008	9.66	2.1269	0.0001	0.87739	0.00003
1390-JP-12-03	Galena-II	17.843	0.003	15.657	0.003	37.951	0.007	9.65	2.1268	0.0001	0.87742	0.00003
1390-JP-12-04	Galena-II	17.840	0.002	15.651	0.002	37.934	0.006	9.64	2.1263	0.0001	0.87727	0.00003
1390-JP-12-05	Galena-II	17.853	0.003	15.662	0.003	37.968	0.008	9.66	2.1267	0.0001	0.87730	0.00003
1390-JP-12-06	Galena-II	17.844	0.003	15.660	0.003	37.959	0.008	9.66	2.1272	0.0001	0.87763	0.00003
1390-JP-12-07	Galena-II	17.851	0.003	15.662	0.003	37.968	0.007	9.66	2.1268	0.0001	0.87735	0.00003
1390-JP-12-08	Galena-II	17.853	0.003	15.662	0.003	37.974	0.007	9.66	2.1270	0.0001	0.87726	0.00003
1390-JP-12-09	Galena-II	17.848	0.003	15.66	0.003	37.961	0.008	9.66	2.1269	0.0001	0.87743	0.00004
1390-JP-12-10	Galena-II	17.857	0.003	15.666	0.003	37.979	0.007	9.67	2.1269	0.0001	0.87733	0.00003
1390-JP-12-11	Galena-II	17.846	0.002	15.66	0.002	37.960	0.007	9.66	2.1271	0.0001	0.87752	0.00003
1390-JP-12-12	Galena-II	17.837	0.002	15.659	0.003	37.951	0.007	9.66	2.1277	0.0001	0.87790	0.00003
1390-JP-12-13	Galena-II	17.838	0.003	15.661	0.003	37.955	0.008	9.66	2.1277	0.0001	0.87790	0.00003
1390-JP-12-14	Galena-II	17.860	0.002	15.662	0.003	37.976	0.007	9.66	2.1263	0.0001	0.87693	0.00003
1390-JP-12-15	Galena-II	17.849	0.002	15.663	0.003	37.968	0.007	9.66	2.1271	0.0001	0.87749	0.00003
1390-JP-12-16	Galena-II	17.857	0.003	15.662	0.003	37.975	0.008	9.66	2.1266	0.0001	0.87705	0.00003

---


$$\mu = {}^{238}\text{U}/{}^{204}\text{Pb}$$

**Table 5 A comparison between the Nayongzhi and the Huize, Tianqiao, and typical MVT deposits**

Characteristics	Tianqiao	Huize	MVT	Nayongzhi
Grade	Pb + Zn: 6.92-20.51 wt. %, Zn/(Zn + Pb): 0.75±	Pb + Zn: 25-35 wt. %, Zn/(Zn + Pb): 0.9±	Pb + Zn: average < 10 wt. %, Zn/(Zn + Pb): 0.8±	Pb + Zn: average 8-10 wt. %, Zn/(Zn + Pb): 0.9±
Tonnage	Pb + Zn total reserve: > 0.2 Mt	Pb + Zn reserve: single ore body ~ 1 Mt, total > 5 Mt	Pb + Zn reserves: single ore body < 1 Mt	Pb + Zn reserves: single ore body < 0.5 Mt, total > 1 Mt
Acreage	The SYG province covers 170, 000 km <sup>2</sup>	The SYG province covers 170, 000 km <sup>2</sup>	Hundreds square kilometers	The Wuzhishan area covers 20 km <sup>2</sup>
Host rocks	Late Devonian and early Carboniferous coarse-grained dolostone	Early Carboniferous coarse-grained dolostone	Cambrian to Carboniferous carbonate rocks	Late Ediacaran and early Cambrian dolostone
Depth of Mineralization	>400 m	>2000 m	<1500 m	<400 m
Tectonic setting	Western Yangtze Block, controlled by the NW fold-thrust fault	Western Yangtze Block, controlled by NE fold-thrust fault	Generally related to extensional basin	Northern Youjiang Basin, controlled by the Wuzhishan anticline
Relation with magmatic activity	Spatially associated with late Permian Emeishan basalts and Mesozoic mafic (diabase) dykes	Spatially associated with late Permian Emeishan basalts	Generally no genetic connection with magmatic activity	No genetic relationship with magmatic activity
Ore-controlled factors	Controlled by thrust fault-fold structure and lithology	Controlled by thrust fault-fold structure and lithology	Mainly controlled by structure and lithology	Mainly controlled by structure and lithology
Age	192 Ma	222-226 Ma	From Proterozoic to Cretaceous	Early Yanshanian
Ore texture and structure	Mainly exhibiting massive structures, and fine-, medium- and coarse-grained textures	Mainly exhibiting massive structures, and fine-, medium- and coarse-grained textures	Exhibiting disseminated, fine granular, branched, colloidal and massive structures and colloidal, skeleton coarse-crystalline textures	Veined, disseminated, and brecciated structures and colloidal, cataclastic, granular textures
Mineral compositions	Sphalerite, galena, pyrite, calcite and dolomite	Sphalerite, galena, pyrite and calcite	Sphalerite, galena, pyrite, barite, fluorite, calcite and dolomite, etc.	Sphalerite, galena, pyrite, calcite, dolomite, quartz and barite
Fluid inclusions	<10 wt. % NaCl equiv.; Cl <sup>-</sup> -Na <sup>+</sup> -Ca <sup>2+</sup> -F <sup>-</sup> -SO <sub>4</sub> <sup>2-</sup> ; 150-280°C	<10 wt. % NaCl equiv.; Cl <sup>-</sup> -Na <sup>+</sup> -Ca <sup>2+</sup> -F <sup>-</sup> -SO <sub>4</sub> <sup>2-</sup> ; 150-300°C	10-30wt. % NaCl equiv.; Cl <sup>-</sup> -Na <sup>+</sup> -Ca <sup>2+</sup> -K <sup>+</sup> -Mg <sup>2+</sup> ; 50-200°C	10-15 wt. % NaCl equiv.; Cl <sup>-</sup> -Na <sup>+</sup> -Ca <sup>2+</sup> -K <sup>+</sup> -Mg <sup>2+</sup> ; 113-232°C
Associated metals	Ag, Cu, Ge, Ga, Cd and In	Ag, Cu, Ge, Ga, Cd and In	Ag	Ag
S isotopes	+8- +15‰	+11-+17‰	+10-+25‰	+11-+33‰
Pb isotopes	Normal Pb isotopes	Normal Pb isotopes	Complicated Pb isotope ratios and regional zonation	Uniform Pb isotope ratios
References	<a href="#">Zhou et al. 2013a, 2014a</a>	<a href="#">Li et al. 2007; Huang et al. 2010</a>	<a href="#">Leach et al. 2005, 2010</a>	<a href="#">Zhu et al. 2016; Jin et al. 2016; This paper</a>